2012

Modeling the Resistance to Hydrostatic Pressures for Superhydrophobic Coatings with Random Roughness

Thomas Michael Bucher Jr.
Virginia Commonwealth University

MODELING THE RESISTANCE TO HYDROSTATIC PRESSURES FOR SUPERHYDROPHOBIC COATINGS WITH RANDOM ROUGHNESS

A thesis submitted in partial fulfillment of the requirements for the degree of Master of Science at Virginia Commonwealth University.

by

THOMAS MICHAEL BUCHER JR.
Bachelor of Science, Mechanical Engineering, Virginia Commonwealth University, 2010

Director: DR. HOOMAN VAHEDI TAFRESHI
ASSOCIATE PROFESSOR, MECHANICAL AND NUCLEAR ENGINEERING

Virginia Commonwealth University
Richmond, Virginia
August 2012

Acknowledgements

I would like to thank my advisor, Dr. Hooman Vahedi Tafreshi, for knowing when to steer me, and when to just let me run. His guidance, his patience, and his mentorship will always be appreciated. Working for him is hands-down the best job I have ever had.

I would also like to acknowledge and thank Dr. Mohamed Gad-el-Hak for the time we worked together on the superhydrophobic project, and for the example his scientific enthusiasm and genuine sense of awe and appreciation for the finer points of fluid mechanics provide. His deep, intimate knowledge of the proper use of hyphens, en dashes, and em dashes will also never be matched—seriously.

I would also like to thank the other members of my committee, Dr. Gary C. Tepper and Dr. Rebecca A. Segal, for what I can only hope will be thoughtful and challenging questions meant to strengthen the work presented in this thesis (I haven't defended it yet as I write this, so I haven't heard their questions).

Of course, I would also like to acknowledge various friends and family throughout my life, living and otherwise, for their love, patience, and inspiration: Bob and Stelle Junod (I'm here because of you, period), Anna and Bud, Mrs. Ward, Gram and Gramp, Laura, Rob, Beth, Mom, assorted Buchers, Junods, Curleys, and everyone else whose name escapes me right now.

For Helen Richard Dyer, my best friend that I don't hang out with ever. Your birthday is a few days after my defense, and all my money just went to pay the bills at the start of the month, so here. I got you a thesis. I hope it's the right size.

Table of Contents

Page

List of Tables

Page

List of Figures

Page

Abstract

MODELING THE RESISTANCE TO HYDROSTATIC PRESSURES FOR SUPERHYDROPHOBIC COATINGS WITH RANDOM ROUGHNESS

By Thomas Michael Bucher Jr., B.S.

A thesis submitted in partial fulfillment of the requirements for the degree of Master of Science at Virginia Commonwealth University.

Virginia Commonwealth University, 2012

Major Director: Hooman Vahedi Tafreshi
Associate Professor, Mechanical and Nuclear Engineering

A superhydrophobic coating can be produced using a hydrophobic material textured with surface roughness on the micro-/nano-scale. Such a coating on the outside of a submersible body may result in reduced skin-friction drag due to a trapped layer of air in the coating. However, this layer may become unstable when subjected to elevated hydrostatic pressures, and a coating's performance is compromised beyond a certain threshold (critical pressure). This thesis presents a numerical model for predicting the pressure tolerances of superhydrophobic coatings comprised of randomly deposited hydrophobic particles or fibers. We have also derived a set of force-balance-based

analytical equations for predicting critical pressure in surfaces with ordered roughness, and compared our numerical model against it, observing reasonable agreement. The numerical model was then applied in a large parameter study, predicting critical pressure for coatings with a given set of microstructure properties.

CHAPTER 1 General Introduction

1.1 Background Information

1.1.1 Superhydrophobicity

The concept of superhydrophobicity emerges from the manner in which a solid surface interacts with water relative to how it interacts with air or other fluids. The interface between two fluids (water and air for this work) that is also in contact with a solid surface forms an angle with the surface (i.e., contact angle) depending on the surface's affinity for one fluid over the other (Dullien, 1992). For the case of a water contact angle less than 90 degrees, the surface is considered to be hydrophilic, and a drop of water will spread across the surface. If the contact angle is greater than 90 degrees, the surface is considered hydrophobic, and a drop of water will instead tend to bead up on the surface. Superhydrophobicity is a special case of hydrophobicity characterized by a contact angle of 150 degrees or more, and low contact-angle hysteresis (deviation in contact angle when the drop is advancing or receding along the surface) (Rothstein, 2010; Samaha *et al*., 2012). As a result, tilting the surface even at a small angle will cause water to roll off the edge (Bhushan, 2012).

Superhydrophobicity is typically the combination of two effects: an inherent hydrophobicity of the surface, and a surface roughness on the micro- or nano-scale which

facilitates the trapping of air beneath a drop of water in the spaces between microridges. This phenomenon is utilized by a number of plants and animals in nature for various purposes. The most famous example is that of the lotus leaf, whose leaves possess a characteristic superhydrophobicity owed to a combination of epidermal roughness and an epicuticular wax coating (Samaha *et al.*, 2012; Koch *et al.*, 2009; Barthlott and Neinhuis, 1997). Figure 1.1a is an image of lotus leaf with a drop of water beaded on its surface (http://yvesrubin.photoshelter.com/image/I0000K.Kp5rcER18). Figure 1.1b is a magnification of the leaf, taken from the work of Koch *et al.* (2009), in which the micro- and nano-scale roughness can clearly be seen. The lotus uses superhydrophobicity for self-cleaning, as an incoming drop will easily roll off the leaf, taking with it any particulate debris in its path. This maximizes the available surface area on the leaf for photosynthesis. Another famous example in nature is the water strider, shown in Figure 1.1c (http://commons.wikimedia.org/wiki/File:Water-strider-1.jpg). In this case, the small, hydrophobic hairs on the insects legs, combined with the increased interface area the legs themselves provide, allow it to walk on the surface of water. A less commonly known example in nature is the diving bell spider, shown in Figure 1.1d (http://www.greendiary.com/gallery/diving-bell-spider). The spider is able to submerge into freshwater, using the hydrophobic hairs on its abdomen and underbelly to carry a small volume of air with it, which it uses to breathe underwater. Moreover, the spider actually builds its web underwater and accumulates a large volume of air from the surface in the web, allowing it to live its entire life underwater, surfacing only briefly once a day or so to replenish its air supply (Seymour and Hetz, 2011).

1.1.2 Superhydrophobic Coatings and Surfaces

The application of superhydrophobicity in nature has led to a great deal of research devoted to studying and understanding its underpinning mechanisms, as well as the production and manufacture of synthetic coatings for industrial and commercial application. Greater water contact angles can be achieved with greater micro-scale surface roughness. Increased roughness reduces the surface area of actual contact between a water droplet and the solid surface, as trapped air within pockets of the surface comprises more of the contact area under the droplet. A higher ratio of water–air contact to total interface surface area (known in the literature as gas fraction) results in an increased free-slip condition and a reduction in the skin-friction coefficient between the droplet and the surface (Samaha *et al.*, 2011b; Rothstein, 2010).

To achieve the necessary surface roughness synthetically, a number of techniques have been developed in the last decade or so. Most engineered superhydrophobic surfaces to date are comprised of micro-fabricated posts or grooves. Figure 1.2a shows a series of SEM images of surfaces comprised of ordered posts from the work of Lee *et al.* (2008). By varying post diameter while keeping pitch (center-to-center distance between posts) constant, the authors were able to determine the gas fraction for each substrate (shown in the corner of each image), and subsequently measure the slip effect for each case using a rheometer. Maynes *et al.* (2007) performed a similar study in which micro-channels were aligned parallel to a passing laminar flow (shown in Figure 1.2b). The ordered nature of

these micro-engineered surfaces lends itself to the devising of analytical functions for meniscus stability based on the balance of forces between the air–water interfaces between the microstructures. These expressions can then be used to compare against numerical and experimental data, as the authors of these works have done. A disadvantage to this manufacturing method is that producing such surfaces and coatings on a large scale is time-consuming, expensive, and impractical when considering the necessity of conforming the surfaces to arbitrary shapes.

The coatings modeled in this thesis are based on superhydrophobic coatings produced via one of two other comparatively inexpensive fabrication techniques. One method involves coating a surface with small hydrophobic particles (aerogel), the combined effect of which produces the necessary nano-scale roughness for superhydrophobicity (Rao *et al.*, 2005). The other method described in this thesis that has been more recently explored involves coating a surface with electrospun nano-fibers (Ochanda *et al.*, 2012a). These techniques are comparatively inexpensive and can conform to arbitrarily shaped surfaces, but the surface roughness they provide is much more random in nature.

1.2 Underwater Application

1.2.1 Drag Reduction

All the works discussed above quantitatively verified the effectiveness of their superhydrophobic surfaces using rheometry. The slip effect can be experimentally measured and represented using slip length. According to Navier's (1823) classical model

for fluid motion, fluid slip velocity and strain rate along the solid surface are proportional. Thus, slip length δ can be determined using (Samaha *et al.*, 2012)

$$\delta = \frac{U_{slip}}{\left(\partial u / \partial y\right)_{wall}} \tag{1.1}$$

where y in this case is the direction normal to flow. Figure 1.3, from the work of Samaha *et al.* (2011a), is a simplified conceptual illustration of slip-length measurement. Fluid flow is generated between two parallel plates spaced at height h from one another, one fixed and one moving, resulting in the well-known Couette-flow profile. The line *S1* represents what the flow profile would be in the case of a no-slip boundary condition on the stationary plate. In the case that the stationary plate has a superhydrophobic coating on it, the free-slip condition facilitated by the high gas fraction where the fluid and plate meet results in a flow profile like that shown as line *S2* in Figure 1.3. The equivalent no-slip condition that would yield a flow profile with the same angle (strain rate) would require the plates to be at height $h + \delta$ from each other. This subtracted height δ is the slip length, which becomes larger as superhydrophobicity increases. With increased slip length (and therefore increased slip velocity) shear stress along the stationary plate is significantly reduced. As a result, moving the top plate at velocity V_{avg} requires less energy.

Among the first uses considered for superhydrophobic surfaces and coatings were self-cleaning for such applications as clothing and car windshields, using the same principles as the lotus. Another interesting application is anti-icing for aircraft. Ice cannot accumulate on the exterior of an airplane if water cannot adhere to the surface to begin with. This

application has also been extended to wind turbines, as the accumulation of ice on the blades causes a considerable reduction in their efficiency (Alizadeh, *et al.*, 2012). However, more recently, the use of superhydrophobic coatings for submersible applications has become a subject of considerable interest (Samaha *et al.*, 2012), and is the specific application studied in this thesis.

For any case of fluid flow over a rigid body, skin-friction drag is unavoidable. Friction drag is a major contributor to the transition of flow to turbulence, which in turn results in increased energy loss and flow-induced noise. While friction drag cannot be eliminated, it can be reduced. A subject of decades-old, ongoing research in the field of fluid mechanics in general is the reduction of skin-friction drag using various active and passive techniques designed to delay the transition to turbulence, and in some cases relaminarize already-turbulent flow. These methods include wall suction and injection, as well as other surface-coating strategies (Gad-el-Hak, 2000). Outfitting the surface of a submersible body with a superhydrophobic coating would allow it to carry a volume of air with it when it is submerged, like the diving bell spider (Figure 1.1d). The free-slip condition this promotes results in less energy necessary to move fluid past the body or vice versa.

1.2.2 Coating Failure

The volume of trapped air that the coating takes with it on submergence is sensitive to several mechanisms that can cause it to degrade. One unavoidable mechanism is simple diffusion of air and water across the interface between them. Given enough time, any

coating made using any method that is submerged in water of any quality will eventually lose its air volume to this phenomenon. Samaha *et al.* (2011a) devised an experimental method to characterize the longevity of a given coating using optical detection of light reflected from the trapped air on a given submerged coating. As the air diffuses into the water, its reflectivity decreases. The salinity of the surrounding water also influences the superhydrophobicity and longevity of a given coating, reducing both as it increases. This effect was studied by Ochanda *et al.* (2012b) using both rheometry and the *in-situ* optical reflection technique from Samaha *et al.* (2011a).

A coating's superhydrophobicity can also be more immediately compromised by increased hydrostatic pressure, which can push the air–water interfaces on the surface deeper into the coating. This increases the solid-contact surface area and reduces the free-slip effect of the coating. The subsequent chapters in this thesis are specifically devoted to this mechanism of coating failure.

There are two primary conditions in which a given superhydrophobic surface in contact with water can be considered to exist in quasi-equilibrium conditions, named after those who first characterized them. The first is the Cassie–Baxter state (or simply Cassie state) (Cassie and Baxter, 1944), illustrated in Figure 1.4. Water rests on top of the surface—or around the entire surface in the case of submergence—with menisci dipping between the posts. The shape and stability of the menisci are governed by the balance of forces acting on them (i.e., applied hydrostatic pressure and opposing surface tension forces), this will

be expanded upon in the next chapter. As pressure increases, the curvature of the menisci becomes sharper, until the critical pressure, beyond which the angle between the air–water interface and the posts reaches the advancing contact angle for the material (Rothstein, 2010), and the system transitions to the Wenzel state (Wenzel, 1936), also shown in Figure 1.4. In the Wenzel state, since the solid-contact surface area is at or near 100 percent, the no-slip boundary condition re-emerges, the superhydrophobicity of the surface is considered to have vanished.

While the description for critical pressure given above is simplified for the case of ordered, microfabricated posts, the same general behavior—a critical pressure beyond which superhydrophobicity fails—applies to any superhydrophobic surface or coating. Describing critical pressure in terms of contributing circumstances of the system is crucial to the use of these coatings in underwater applications, and to the understanding of their limits. For the simple case of ordered posts, Zheng *et al.* (2005), and later Lee and Kim (2009), devised an analytic expression based on the balance of forces at the menisci to predict critical pressure. This relation will be derived in the next chapter. Samaha *et al.* (2011b) used the relation of Lee and Kim (2009) as a basis for numerically predicting critical pressure for a surface with randomly distributed posts, using the famous Voronoi diagram to establish local post spacing and gas fractions (Okabe *et al.*, 2000). Later, Emami *et al.* (2011) derived and numerically solved a differential equation for meniscus shape and stability in a superhydrophobic surface comprised not only of randomly

distributed posts, but of posts with arbitrary sizes and heights as well, revealing critical pressure, as well as the location of initial coating failure.

The analytical and numerical models presented so far can be applied to any superhydrophobic surface comprised of microfabricated, cylindrical posts. However, if the surface roughness is produced using aerogel particles, fibers, or posts whose cross-sectional area—and therefore gas fraction— varies along their height (e.g., cone-shaped posts or posts that are thinner at their base), modeling their behavior becomes more complex, as the gas fraction is no longer independent of coating depth. Tuteja *et al.* (2008) produced a model for predicting critical pressure for surfaces comprised either of ordered, parallel fibers (cylinders) or "micro-hoodoos" (posts shaped like the head of a nail). This model, however, uses simplifying assumptions (such as only one layer of fibers with a flat surface directly under them) that limits its applicability to highly ordered cases—and only one layer of parallel fibers, no more. Emami *et al.* (2012) extended the same methodology used for posts to thin superhydrophobic coatings comprised of nano-fibers in random orientations, projecting a thin layer of such fibers into two dimensions for meniscus analysis. While nonetheless accurate from a force-balance perspective, the resolving of the top few fibrous layers to a two-dimensional projection eliminates the curvature of the fibers and consideration of subsequent fiber layers, thus limiting its use to thin coatings comprised only of several layers.

1.3 Objective of this Thesis

This thesis presents a numerical model for predicting the critical pressure for superhydrophobic coatings produced using either aerogel particles or electrosupn nano-fibers. These coatings, while able to be produced at a fraction of the cost of microfabricated posts and the like, and able to conform to arbitrary surfaces, possess random surface roughness, and the disordered distributions of particles or fibers result in much more arbitrary pore shapes and sizes. Thus, they do not so easily lend themselves to analytical correlation to describe their behavior.

As an alternative, this thesis uses the so-called Full-Morphology (FM) simulation technique to characterize a coating's resistance to a given hydrostatic pressure based on its geometry. Since the method is not purely based on the balances of forces for a specific coating, it gives only an approximation of a given coating's resistance to pressure. For simple cases such as ordered parallel fibers and ordered spheres, it is possible to directly compare the FM method with the force-balance method—and such comparisons are made in this thesis. However, once the distribution of the fibers or particles is no longer ordered, no analytical expression can be used. The FM method presented here not only extends to randomly ordered fibers or particles, but is able to predict the effect that individual parameters (e.g., porosity, particle size, fiber diameter, etc.) have on the critical pressure of a given coating.

Chapter 2 focuses on coatings produced by coating a surface with aerogel particles. First the force-balance equation for the simple case of ordered, microfabricated, cylindrical posts from the work of Zheng *et al.* (2005) is derived and compared with the FM method. The derivation is then extended, presenting the balance of forces for the case of ordered spheres, to compare against FM, before then presenting FM results on coatings comprised of randomly distributed spheres with varying parameters.

Chapter 3 is devoted to coatings comprised of electrospun nano-fibers. Within this manufacturing technique, however, we explore two methods that result in two different types of fiber orientation: one that is layered with randomly deposited fibers oriented in any direction within their respective layers; and one with fibers in a layer oriented parallel to one another, and each layer oriented orthogonally to the adjacent layer. Both coating types are described in detail and investigated. We again first derive the force-balance equation for the case of ordered, parallel cylinders, and then compare it to the FM method for various cases. We also compare these two methods with the parallel-cylinder correlations of Tuteja *et al.* (2008). From there, an extensive parameter study reveals the relative effects of various microstructure properties on the pressure tolerances of various nano-fiber coatings. We include bimodality (fibers with two different diameters in one coating) in the subsequent parameter study, as adding coarse fibers to a coating has advantages that will be discussed in the chapter.

Chapter 4 will present the conclusions for the work performed in this thesis, and give thoughts regarding future studies that could stem from this work.

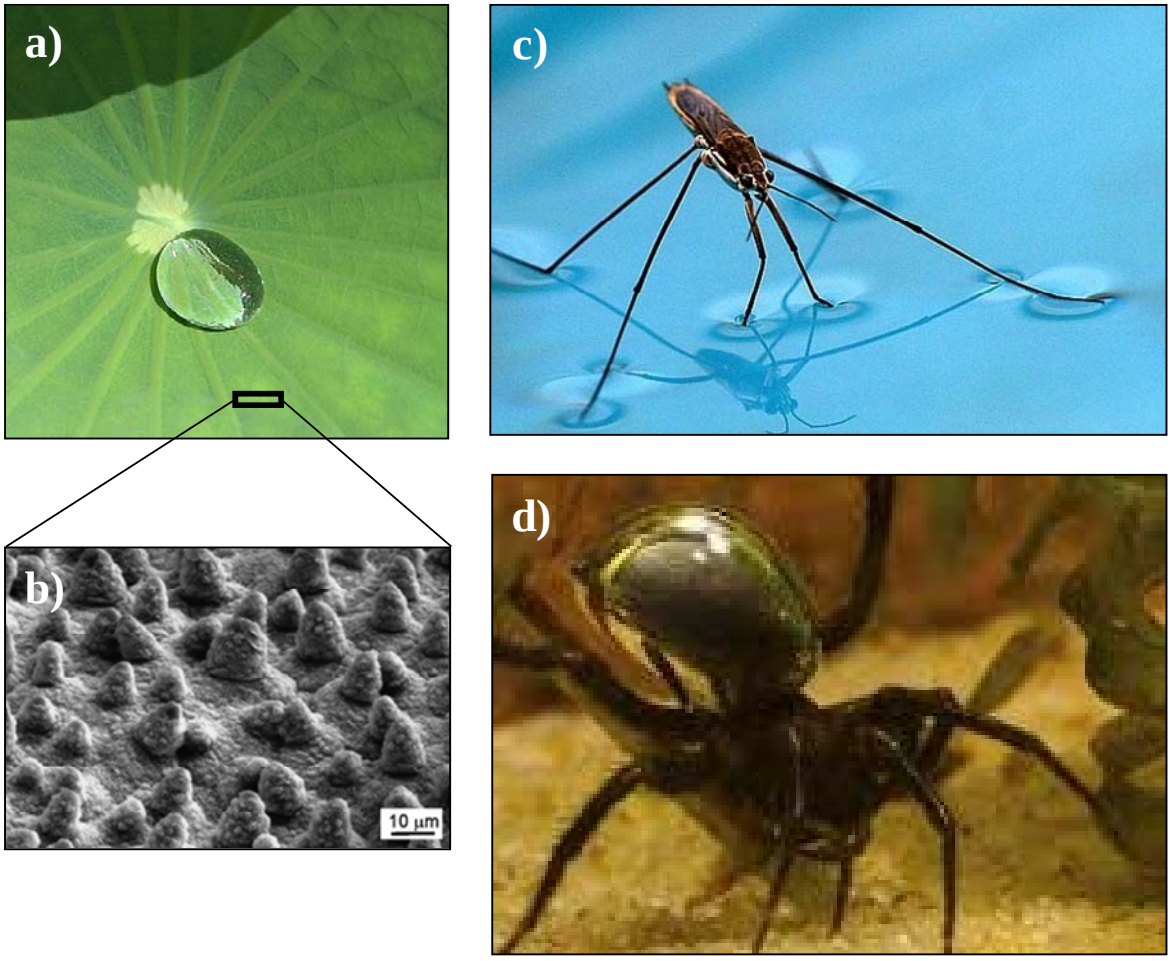

Figure 1.1: Example applications of superhydrophobic surfaces in nature: (a) a lotus leaf[1] using superhydrophobicity for self-cleaning; (b) magnification of the lotus leaf to illustrate micro- and nano-roughness, taken from the work of Koch *et al.* (2009); (c) a water strider[2] walking on water; (d) a diving bell spider[3] using trapped air on its abdomen and underbelly to breathe underwater.

[1] Image from http://yvesrubin.photoshelter.com/image/I0000K.Kp5rcER18
[2] Image from http://commons.wikimedia.org/wiki/File:Water-strider-1.jpg
[3] Image from http://www.greendiary.com/gallery/diving-bell-spider

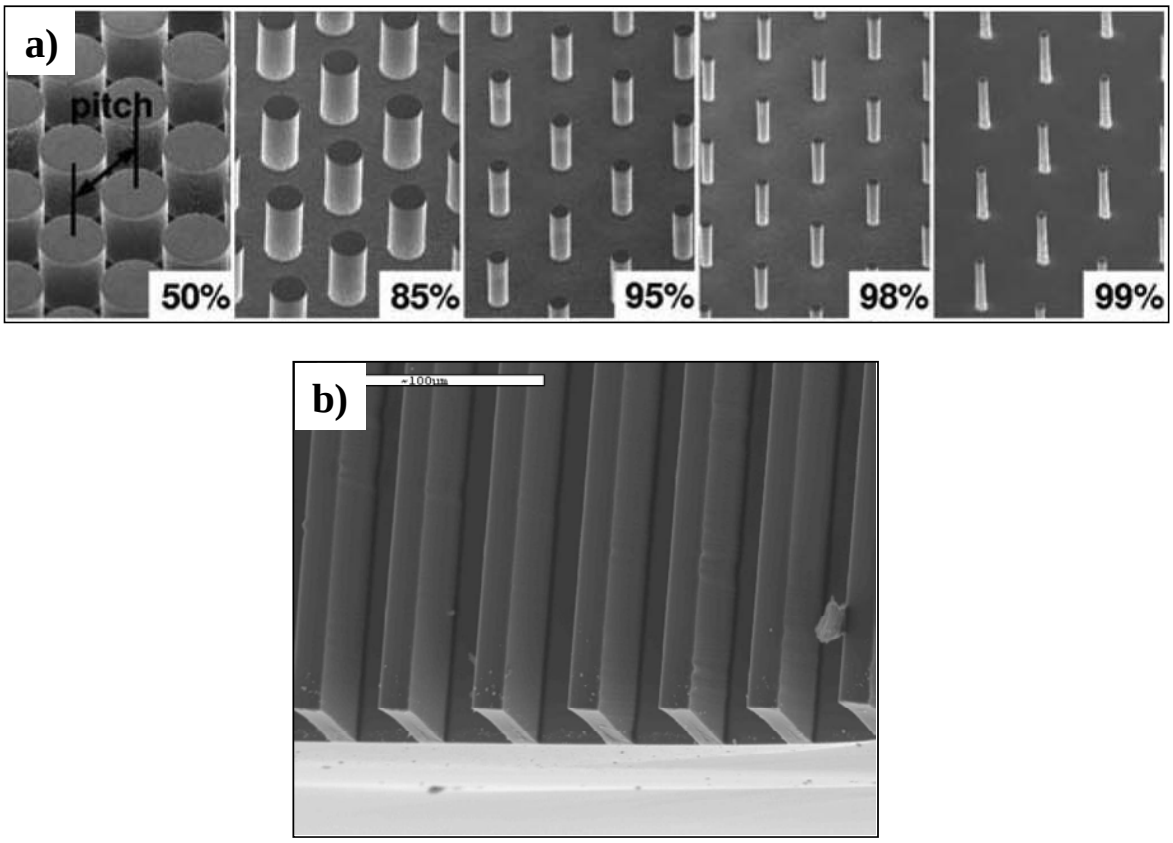

Figure 1.2: (a) Examples of superhydrophobic surfaces comprised of evenly distributed, microfabricated posts under an SEM from the work of Lee *et al.* (2008). The pitch for all surfaces shown is 50 μm. Percentages denote the gas fraction for each case. (b) SEM image of a surface comprised of microfabricated grooves from the work of Maynes *et al.*, (2007). The grooves are 15 μm deep and 30 μm wide, while the ridges have a width of 10 μm.

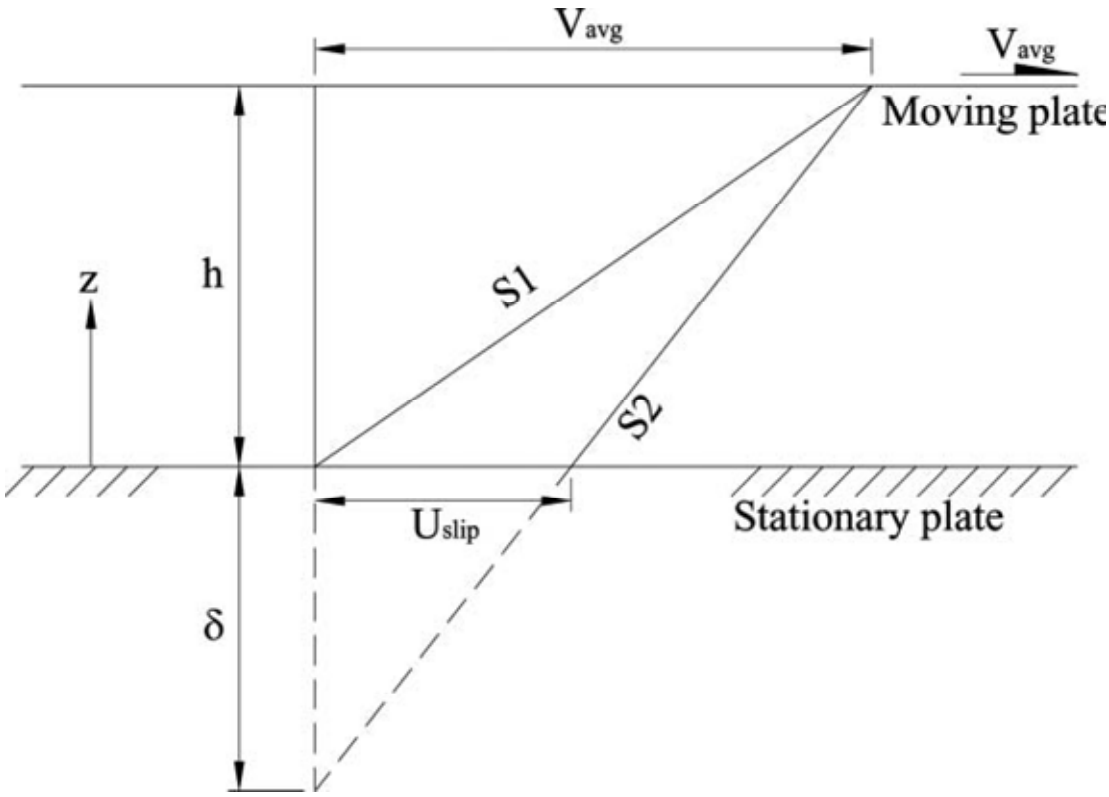

Figure 1.3: Conceptual illustration of the difference between the no-slip (line *S1*) and slip (line *S2*) boundary conditions for the flow profile of a fluid trapped between two parallel plates, one fixed and one moving. Image is from the work of Samaha *et al.* (2011a).

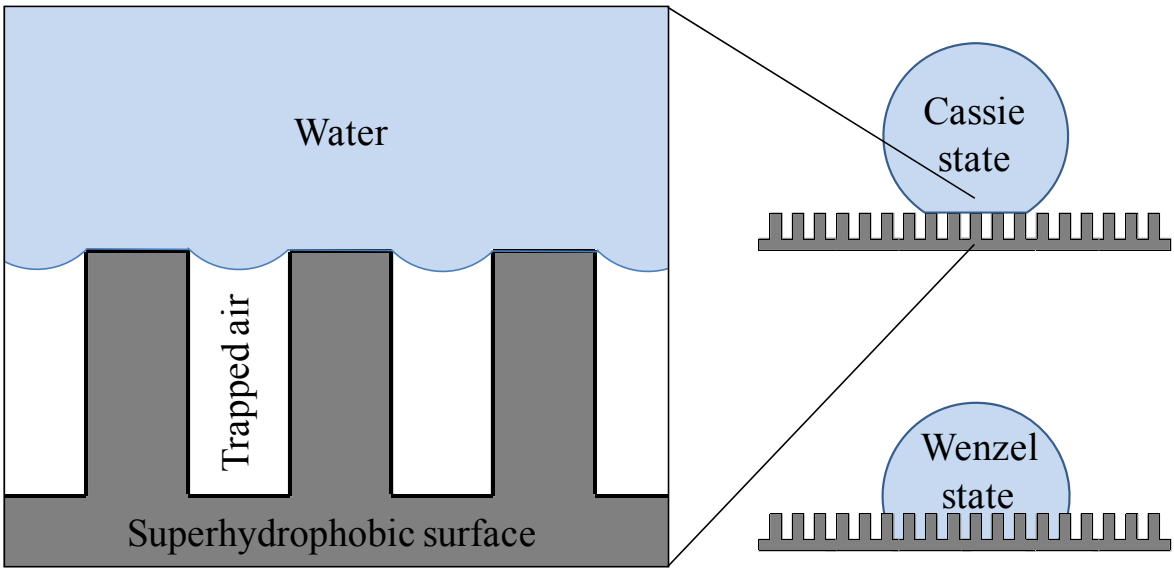

Figure 1.4: Side view illustrating the two primary quasi-static water–surface interface states on a superhydrophobic surface, in this case comprised of ordered, microfabricated posts.

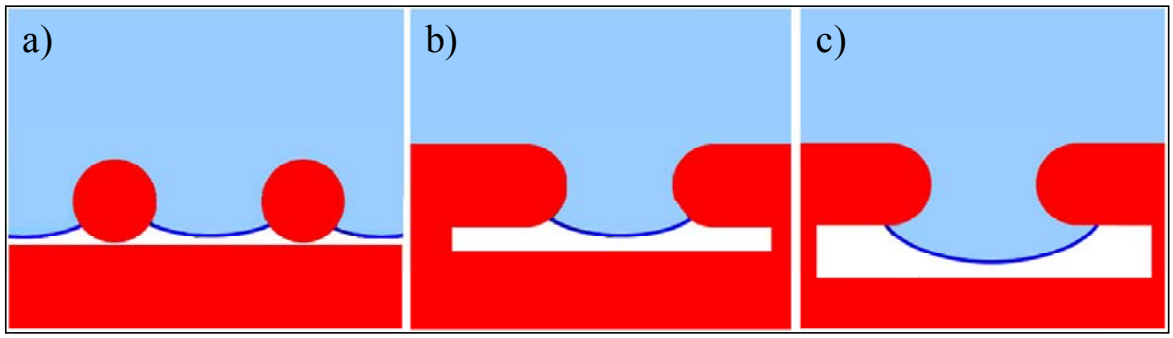

Figure 1.5: Example cross-sectional illustrations of the air–water interface for superhydrophobic surfaces comprised of micro-structures other than cylindrical posts from the work of Tuteja *et al.* (2008): (a) Surface consists of one layer ordered parallel cylinders (oriented into the page); (b) Surface comprised of "micro-hoodoos" (resembling protruding pushpins) set low enough for the meniscus to touch the bottom surface at sufficient pressure before it breaks; (c) Surface comprised of "micro-hoodoos" set high enough such that the meniscus will not touch the bottom before it breaks.

CHAPTER 2 Modeling Resistance of Granular Superhydrophobic to Hydrostatic Pressures[4]

2.1 Overview

It is known that a combination of hydrophobicity and micro- or nano-scale surface roughness can result in superhydrophobicity. This is because a rough hydrophobic surface can entrap the air in its pores, resulting in reduced contact between water and the frictional solid walls. From a macro-scale viewpoint, this causes a reduction in the overall drag force exerted on the surface. From an engineering standpoint, superhydrophobic surfaces can be exploited to reduce the drag force exerted on submerged moving objects such as ships, submarines, or torpedoes.

When the pores in a superhydrophobic surface are filled with air, the system is considered to be at the Cassie state (Cassie and Baxter, 1944). If the pressure is high, water may penetrate into the pores of the surface and displace the air. This results in the elimination of the superhydrophobicity, and transition to the so-called Wenzel state (Wenzel, 1936). The

[4] The contents of this chapter is published in an article entitled "Simulation of meniscus stability in superhydrophobic granular surfaces under hydrostatic pressure," by B. Emami, T.M. Bucher, H. Vahedi Tafreshi, D. Pestov, M. Gad-el-hak, and G. Tepper, Colloids and Surfaces A-Physiochemical and Engineering Aspects **385**, 95–103 (2011); and in part in "Modeling resistance of nanofibrous superhydrophobic coatings to hydrostatic pressures: the role of microstructure," by T.M. Bucher, B. Emami, H. Vahedi Tafreshi, M. Gad-el-hak, and G. Tepper, Physics of Fluids **24**, 022109 (2012).
.

pressure at which a superhydrophobic surface departs from the Cassie state is here on referred to as the critical pressure (Sheng and Zhang, 2011).

Superhydrophobic surfaces are usually manufactured by microfabrication of grooves or posts on a hydrophobic surface. Hence, most of the theoretical studies in the literature correspond to microfabricated surfaces (Gao and Feng, 2009; Lauga and Stone, 2003; Martell *et al*., 2009; Davies *et al*., 2006; Maynes *et al*., 2007; Sbragaglia and Prosperetti, 2007) and experimental (Daniello *et al*., 2009; Ou *et al.*, 2004; Ou and Rothstein, 2005; Rothstein, 2010; Truesdell *et al.*, 2006). Microfabrication, however, is a costly process and cannot be easily applied to large surfaces with arbitrary shapes. An alternative approach to produce a superhydrophobic surface is by depositing hydrophobic particles on a substrate. Our group, among many others (Doshi *et al.*, 2005, Ma *et al.*, 2005 and 2008; Rao *et al.*, 2004a and b; Singh *et al.*, 2005; Zhu *et al.*, 2006), is currently active in producing and characterizing granular superhydrophobic surfaces. As will be discussed in the next section, such coatings can be produced at a much lower cost and can better conform to the surface of objects with arbitrary shapes. Coatings produced by randomly deposited particles do not, however, provide a precise control over the surface microstructure, and are more susceptible to elevated pressures (Samaha *et al.*, 2011b).

As mentioned earlier, the major problem in utilizing superhydrophobic surfaces for submersible applications is that the slip effect diminishes under elevated hydrostatic pressures (i.e., depths). The objective of the study presented in this chapter is, therefore, to

better our understanding of the importance of microstructural parameters such as particle size or porosity on the superhydrophobic performance of such coatings under elevated hydrostatic pressures. In this chaper, we only consider surfaces made up of granular materials.

In the next section, we present a superhydrophobic surface made up of ground aerogel particles as an example of granular superhydrophobic surfaces. In Section 2.3, we present an analytical formula that we have derived for predicting the critical pressure of superhydrophobic surfaces. In Section 2.4, we describe the numerical scheme that considered for conducting our 3-D simulations. This section also contains a series of simulations that are performed to ensure that our results are not affected by statistical errors or simulation artifacts. Our results and discussions are given in Section 2.5 where we compare the predictions of our analytical formula with the results of 3-D simulations. In this section we also present a parameter study to compare performance of coatings with different microstructural parameters. This discussion is followed by our conclusions in Section 2.6.

2.2 Superhydrophobic Surfaces Made Up of Aerogel Particles

As mentioned earlier, a superhydrophobic surface can simply be produced by depositing randomly distributed hydrophobic particles on a sticky solid surface. For demonstration purposes here, we have produced a granular superhydrophobic surface by grinding trimethylsilylated aerogel (consisting of $(CH_3)_3Si$- groups) particles and depositing them

onto an adhesive surface. The average diameter of the ground aerogel particles was measured using an optical microscope and was about 20 to 100 micrometers. To test the hydrophobicity of our aerogel coating, a water droplet was placed on the surface and its contact angle was measured using an optical microscope. Figure 2.1a is an optical-microscope image of our aerogel coating, and Figure 2.1b is a photograph of a water droplet placed on the aerogel coated surface. The aerogel coating explored in this work is only an example of such surfaces. As will be discussed later in this chapter, our numerical simulations are also aimed at providing guidelines for design and optimization of the coating microstructure in terms of particles size and thickness of the coating, as well as its porosity and randomness.

2.3 Analytical Formula

By applying balance of forces, an analytical relationship was proposed for predicting the stability of the meniscus formed between the cylindrical posts on a microfabricated superhydrophobic surface (Zheng *et al.*, 2005; Lee and Kim, 2009). Here, we extend this analytical relationship to superhydrophobic surfaces with ordered spherical particles. In the following subsections, the above method is briefly described for the case of cylindrical posts arranged in aligned configurations.

2.3.1 Surfaces with ordered posts

An ordered array of vertical cylinders representing the posts on a microfabricated superhydrophobic surface, is shown in Figure 2.2. The diameter of each post is denoted by

d_p, and the pitch (center-to-center distance) between each two adjacent posts is denoted by L_p. In Figure 2.2, we also show the balance of forces for the meniscus surrounding a given post. Here, F_σ and F_σ' denote the surface tension forces applied to the two sides of the interface, and p represents the pressure applied from the liquid side minus the pressure on the gas side, which is assumed to be equal to the atmospheric pressure, P_∞. By applying balance of forces in the z-direction and considering that $F_\sigma = \sigma\pi d_p$, one obtains

$$p\left(L_p^2 - \frac{\pi d_p^2}{4}\right) = -\sigma\pi d_p \cos\theta \tag{2.1}$$

where θ is the liquid–solid contact angle. Note that F_σ' does not have any component in the z-direction due to the symmetrical arrangement of the posts. The above equation yields the critical pressure beyond which the superhydrophobicity of the surface vanishes. This is because, unlike the case of granular surfaces (see the next section), the cross-section of the posts does not change in the z-direction, and so the surface tension forces do not change when the interface moves downward along the posts. The critical pressure can then be obtained as

$$p^* = \frac{-4\pi\sigma d_p \cos\theta}{4L_p^2 - \pi d_p^2} \tag{2.2}$$

Equation (2.2) was reformulated by Lee and Kim (2009) in terms of the gas area fraction of the superhydrophobic surface:

$$p^* = \frac{-2\sigma\cos\theta\sqrt{\pi(1-\phi_g)}}{\phi_g L_p} \tag{2.3}$$

where $\phi_g = \frac{4L_p^2 - \pi d_p^2}{4L_p^2}$ is the gas area fraction. As granular porous coatings are better described in terms of solid volume fraction (SVF), we reformulated Equation (2.2) in terms of SVF for convenience.

$$p^* = \frac{-4\varepsilon\sigma\cos\theta}{d_p(1-\varepsilon)} \tag{2.4}$$

where ε is equal to SVF for the surface with ordered posts, and is calculated as

$$\varepsilon = \frac{\pi d_p^2}{4L_p^2} \tag{2.5}$$

Recall that this analytical solution has also been extended to superhydrophobic surfaces with randomly distributed posts of dissimilar diameters, heights, and materials (Emami *et al.*, 2011).

2.3.2 Surfaces with Ordered Spheres

In this section, we derive an expression for critical pressure for superhydrophobic surfaces made up of orderly packed spherical particles (see Figure 2.3). Here, we also show the balance of forces for the meniscus surrounding a given particle. The interaction between the meniscus and hydrostatic pressure is more complicated here in comparison to that of

ordered posts. This is because the cross-section of the spheres changes as the meniscus moves downward in the *z*-direction. Therefore, magnitude of the surface tension force F_σ changes depending on the height at which the meniscus is located, characterized by the angle α, as can be seen in Figure 2.3. By applying balance of forces in the *z*-direction, and considering that $F_\sigma = \sigma\pi d_s \sin\alpha$, one obtains

$$p\left(L_s^2 - \frac{\pi d_s^2}{4}\sin^2\alpha\right) = \pi\sigma d_s \sin\alpha \cos\left(\frac{3\pi}{2} - \theta - \alpha\right) \tag{2.6}$$

where θ is the liquid–solid contact angle, i.e., the angle between the interface and the tangent line to the sphere surface. In this equation, d_s is the sphere diameter and L_S is pitch between two adjacent spheres. Again, note that due to symmetric arrangement of the spheres, F_σ' does not have any component in the *z*-direction. The critical pressure for the case of ordered spheres can then be obtained as

$$p^* = \frac{4\pi\sigma \sin\alpha^* \cos\left(\frac{3\pi}{2} - \theta - \alpha^*\right)}{d_s\left[4\left(\frac{\pi}{6\varepsilon}\right)^{2/3} - \pi\sin^2\alpha^*\right]} \tag{2.7}$$

where SVF is given as

$$\varepsilon = \frac{\pi d_s^3}{6L_s^3} \tag{2.8}$$

and α^* is a critical angle at which the surface tension force, and therefore the hydrostatic pressure *p,* is maximum. The surface departs from the Cassie state at the critical angle α^*, because the hydrostatic pressure becomes larger than the surface tension force beyond this point, and so the meniscus can no longer withstand the pressure. As a result, at least the first layer(s) of the particles becomes immersed in water. This can affect the drag reduction significantly. As a result, the superhydrophobicity starts to diminish. The critical angle can be obtained by setting $\left.\frac{dp}{d\alpha}\right|_{\alpha=\alpha^*}$ equal to zero.

$$\begin{aligned}&\left[\cos\alpha^*\cos\left(\frac{3\pi}{2}-\theta-\alpha\right)+\sin\alpha^*\sin\left(\frac{3\pi}{2}-\theta-\alpha^*\right)\right]\left(4-\pi\varepsilon^{2/3}\sin^2\alpha^*\right)\\&+2\pi\varepsilon^{2/3}\sin^2\alpha^*\cos\alpha^*\cos\left(\frac{3\pi}{2}-\theta-\alpha^*\right)=0\end{aligned} \tag{2.9}$$

As can be seen from Equation (2.9), the critical angle is only a function of SVF, assuming that the surface tension and liquid–solid contact angle are constant. Figure 2.4 shows the critical angle α^* calculated at different SVFs. As can seen, α^* is slightly larger than $\pi/2$ for all of the cases, and decreases as SVF increases.

2.4 Numerical simulations

The analytical expressions discussed in Section 2.3, are developed for simplified geometries in which particles are arranged in an ordered configurations. To study performance of superhydrophobic coatings made up of randomly distributed particles, we consider a numerical method based on Full-Morphology (FM) (Hazlett, 1995; Hilpert and

Miller, 2001). In the FM method, a quasi-static distribution of liquid and gas, water and air in the present work, is calculated in a 3-D domain at a given capillary pressure. The calculations are carried out for a range of capillary pressures, and so a relation between the capillary pressure and liquid (or gas) saturation is obtained. This method has also been used for calculation of pressure–saturation relationships in porous media (Jaganathan *et al.*, 2008; Ashari and Tafreshi, 2009; Ashari *et al.*, 2010). The FM method is implemented in this thesis using the GeoDict code developed by Math2Market GmbH (www.geodict.com), Germany.

The underlying principle of the FM method is that at a given capillary pressure p_c the pore space accessible to the non-wetting phase (water in this work) is determined by the pore size via the Young–Laplace equation,

$$p_c = -\frac{2\sigma\cos\theta}{r} \tag{2.10}$$

Figure 2.5 shows a sample domain consisting of nano-fibers, providing a visual demonstration of a progressing FM simulation. When calculations are carried out for an adequate range of capillary pressures, a relation between capillary pressure and liquid (or gas) saturation is obtained. The FM method uses a sphere-caging algorithm, and has also been used for calculation of pressure–saturation relationships in fibrous media with different microstructures in (Jaganathan *et al.*, 2008, Ashari and Tafreshi, 2009; Ashari *et al.*, 2010). This is achieved by considering one face of a given cubic domain as the non-

wetting reservoir (the top face in Figure 2.5). For each incremental pressure rise in the non-wetting reservoir, the FM algorithm determines a minimum pore radius (i.e., sphere radius) using the Young–Laplace equation (Equation 3.3), and examines every voxel in the domain. If a voxel is not occupied by a fiber, along with every voxel around it corresponding to the given minimum sphere radius, and if an unbroken path exists between that voxel and the reservoir face into which other spheres of at least this minimum radius can fit in the same manner, then a sphere is placed with that voxel as its center, with a radius equal to the distance between the voxel and the nearest solid object. A sphere must be connected via other spheres to the reservoir. The overlying spheres form the non-wetting fluid continuum. This process is repeated for every following pressure increment, with a smaller minimum sphere radius used each time pressure is raised.

Obviously, as is the case in an actual fluid drainage experiment, the non-wetting phase can only penetrate into a porous medium as deeply as the most constrictive spaces therein—the size and distribution of which being a function of the coating's microstructure—allow (the famous ink-bottle effect) (Jaganathan *et al.*, 2008). More detailed explanation of the full-morphology method can be found in the literature (Hilpert and Miller, 2001; Schultz *et al.*, 2007; Becker *et al.*, 2008, Vogel *et al.*, 2005). The red spheres are overlaid with one another to form a virtual fluid continuum within the medium, as it appears in Figure 2.5. Even if larger spaces exist inside the coating, the non-wetting front will not be able to reach them if a prohibitively tight space must first be cleared. When no more spheres of the prescribed radius can be fitted into the available domain, water saturation is calculated

based on the volume of space thus occupied. The process is then repeated using a smaller sphere radius, corresponding to the next ascending input capillary pressure value. The superhydrophobic coatings presented in this chapter (which consist of either posts or spherical particles) can be considered as porous media. Thus, the FM approach can be used to calculate the critical pressure; this will be explained more clearly in Section 2.5.

2.5 Results and Discussion

This section is divided into four parts. In Section 2.5.1, the numerical results for the superhydrophobic surfaces with ordered posts are explained and compared to the analytical relation (Zheng *et al.*, 2005). This is followed by Section 2.5.2, where the numerical results for the superhydrophobic surfaces with ordered spheres are presented and compared to our analytical method. In Section 2.5.3, the results of the randomly distributed spheres are explained. Finally, we revisit our force-balance method from Section 2.3, extending it to the case of randomly distributed spheres in Section 2.5.4.

2.5.1 Surfaces with ordered posts

In this section, we considered arrays of ordered posts with a diameter of d_p = 100 μm, and a center to center distance of $102 < L_p < 250$ μm corresponding to a range of SVFs $0.13 < \varepsilon < 0.75$. A liquid–solid contact angle of $\theta = 120^o$ was arbitrarily chosen for all the simulations reported here. Due to the inherent symmetry of such ordered geometries, we have considered a domain comprised of 9 posts (9 unit cells) for better visualization, as shown in Figure 2.6. The top and bottom boundaries of the domain are assumed to be

connected to water and air reservoirs, respectively, whereas a symmetry boundary condition is applied to the lateral sides of the domain. Note that blue represents the posts and red represents water; air is clear. The SVF of the surface shown in this figure is ε = 0.46. Figure 2.6a represents the domain at any pressure below p_c = 1775 Pa, which is below the critical pressure and no water intrusion is observed. At a hydrostatic pressure of p_c = 1775 Pa and above, water starts to intrude into the domain (see Figure 2.6b), and since the pore size is invariant with the length of the posts, water fills up all the pores at once. Later in this chapter we will see that this does not happen in the case of granular surfaces.

The sudden intrusion of water between the posts can be better seen in Figure 2.7, where we show the simulation results for the pressure vs. water saturation (i.e., the water filling ratio). The inset figure shows a close-up of the results for water saturation up to 0.1; the results clearly show that water does not penetrate between the posts when the pressure is lower than the critical pressure; as pressure increases beyond this point, water saturation increases rapidly, and so superhydrophobicity of the surface vanishes. Note too that the water saturation increases rapidly from almost zero to 0.6 at above the critical pressure, but only increases slowly with increasing pressure beyond this point. This is because the Full-Morphology method calculates a capillary radius (size of a spherical object) at any given capillary pressure, and uses these spheres to fill up the pore space. By increasing the pressure at each step of the simulation, the capillary radius decreases incrementally, allowing smaller pores to be filled. For the case of ordered posts shown in Figure 2.7 at the critical pressure, the size of the spheres that fill most of the pore space between the posts is

relatively large. To fill the remaining pore space after a saturation of about 0.6, smaller spheres (higher pressures) are needed. This can be seen in Figure 2.6 (corresponding to a saturation of 0.6) where the space between the blue posts are partially filled with water), but there are still some air-filled volumes.

We have compared predictions of our FM simulations with the analytical expression of Zheng *et al.* (2005)—Equation 2.4—for surfaces made up of vertical posts having a diameter of 100 μm but different SVFs (post spacings) in Figure 2.8. As one would expect, critical pressure increases with SVF as it causes the distance between the posts to decrease. Note that the lack of perfect agreement between the two curves is attributed to the fact that the full-morphology method is purely geometrical and so its predictions depend only on the capillary radius at any given pressure. The analytical method, on the other hand, is more complicated in physics (i.e., more realistic), and accounts for the balance of forces on the air–water meniscus. Recall, however, that full-morphology is the only viable method for conducting such calculations when working with surfaces with random microstructure, where all other analytical methods fall short.

It is also worth mentioning that we have run a series of simulations with different voxel sizes to ensure that the results presented here are independent of the size of computational cells. Figure 2.9, for example, shows the critical pressure computed for a domain with ε = 0.35, by simulations at $\Delta = d_p/2$ to $d_p/50$, where Δ is the voxel size. As can be seen, at a voxel size of $\Delta = d_c/5$ the calculations seem to become more or less independent of the

voxel resolution. In all of the simulations presented in this chapter, we use a voxel size $\Delta < d_c/5$ to eliminate any numerical errors associated therewith.

2.5.2 Surfaces with ordered particles

As mentioned earlier in Section 2.3.2, we have proposed an analytical expression for predicting the critical pressure in superhydrophobic surfaces made up of granular materials packed in an ordered configuration (Equation 2.7). In this section we compare predictions of our new expression with those of the FM method.

In our FM simulations, we considered arrays of ordered spheres with a sphere diameter of $d_s = 100$ μm, and a pitch of $102 < L_s < 250$ μm corresponding to a range of SVFs $0.03 < \varepsilon < 0.49$. A liquid–solid contact angle of $\theta = 120^o$ is arbitrarily chosen for all the simulations reported here. Due to the inherent symmetry of such ordered surfaces, we have considered a domain comprised of 64 spheres (arrays of $4 \times 4 \times 4$ spheres) for better visualization, as shown in Figure 2.10. Similar to the ordered post simulations, top and bottom boundaries of the domain (normal to the z-axis) are assumed to be connected to water and air reservoirs, respectively, and symmetry boundaries are applied to the lateral sides. The SVF of the surface shown in this figure is $\varepsilon = 0.49$. Figure 2.10a–d represents the domain at the pressures of $p = 0$, 2500, 3200, and 3500 Pa, respectively. As can be seen, at atmospheric pressure ($p = 0$), there is no intrusion of water between the particles. As the hydrostatic pressure increases beyond the atmospheric pressure, water starts to intrude gradually into the domain, as can be seen in Figure 2.10b and c. The results clearly show

that, unlike surfaces with ordered posts, water does not fill up all the pores at once. As the hydrostatic pressure increases beyond p = 3200 Pa, water saturation increases rapidly with pressure, and so water fills up the whole domain, as can be seen in Figure 2.10d.

This behavior is better shown in Figure 2.11, which represents the simulation results for the pressure vs. water saturation. The results clearly show that water saturation increases gradually with pressure for p < 3200 Pa. Beyond p = 3200 Pa, water saturation increases rapidly with any slight increase of pressure, and so water fills up almost the whole domain. This is the pressure at which superhydrophobicity of the surface vanishes, namely the critical pressure p^*; we refer to the corresponding saturation as critical saturation S^*.

Turning back to Figure 2.10c, it can be seen that the critical pressure corresponds to when half of the first layer of spheres is wetted by water. From a numerical point of view, this point corresponds to the smallest gap between two adjacent spheres; once the capillary radius r is small enough to fill this gap, then the rest of the domain is filled with water rapidly. This explains the jump of water saturation that can be observed by comparing Figures 2.10c and d. This behavior is also confirmed by our analytical method, because the angle α calculated from Equation 2.9 is found to be close to $\pi/2$ for all of the cases studied in this paper. Note that the slight difference between the numerical and analytical values of α is due to the fact that the numerical method is purely geometrical, while the analytical method is based on balance of forces; the maximum capillary force does not always occur at $\alpha = \pi/2$. It can be shown that the water saturation when half of the first layer is wetted, i.e. the critical saturation, can be calculated as

$$S^* = \frac{1}{2N^{1/3}} \tag{2.13}$$

where N is the total number of spheres, and so $N^{1/3}$ is the number of spheres in each row. Note that Equation 2.13 holds for a cubic domain, with all the domain dimensions being equal.

We have compared predictions of our FM simulations with our analytical expression, Equation 2.7, for surfaces made up of spherical particles having a diameter of 100 μm but different SVFs (sphere spacing) in Figure 2.12. As one would expect, the critical pressure increases with SVF as it causes the distance between the spheres to decrease. Note that the agreement is less perfect, perhaps because the resolving the menisci's actual curvature becomes more important at higher SVFs—something which is not properly modeled by the FM method. Nevertheless, our numerical and analytical results are in relatively good agreement. We can now use FM simulations to predict the critical pressure of a superhydrophobic surface with randomly distributed spherical particles, as explained in the next section.

Note that, similar to the ordered posts simulations, we have run a series of simulations with different voxel sizes to ensure that the results presented here are independent of the mesh resolution. The results are independent of domain size, given the symmetry of the system.

2.5.3 Surfaces with randomly distributed particles

In an actual superhydrophobic surface produced using aerogel, the spherical particles are randomly distributed on the top of each other. We used FM simulations to calculate the critical pressure of superhydrophobic surfaces with randomly distributed spherical particles. In our simulations, we considered domains consisting of randomly distributed spherical particles with a diameter of d_s = 100 μm, with a range of SVFs $0.16 < \varepsilon < 0.34$. Figure 2.13 shows an example of our results for a domain of randomly distributed spheres, which corresponds to a SVF of 0.34. In random generation of domains, the spheres were allowed to touch, but not to penetrate into each other. The boundary conditions were similar to the ordered sphere simulations. Figure 2.13a–d represents the domain at the pressures of p = 0, 600, 1000, and 2000 Pa, respectively. As can be seen, at the atmospheric pressure (p = 0), there is no intrusion of water between the particles. As the hydrostatic pressure increases beyond the atmospheric pressure, water starts to intrude gradually into the domain, as can be observed in Figure 2.13b and c. Unlike the case of ordered spheres, water does not penetrate homogenously over the surface, but penetration starts at locations with larger pore space. As the hydrostatic pressure further increases, water fills up the whole domain, as shown in Figure 2.13-D.

As mentioned earlier, the critical pressure for ordered spheres was found to occur at the point that half of the first layer of spheres is wetted by water. For a domain of randomly distributed particles, on the other hand, the spheres are not positioned in a layered form. Hence to avoid underestimation of the critical pressure and the critical saturation, we

assume that the critical saturation of a superhydrophobic surface with randomly distributed spheres corresponds to the point where the first layer is completely immersed in water, if the distribution of the spheres were ordered. The critical saturation S^* can then be calculated as

$$S^* = \frac{1 - 2\varepsilon + \left(6\varepsilon / \pi\right)^{1/3}}{2N\left(1-\varepsilon\right)} \tag{2.14}$$

The corresponding pressure, i.e. the critical pressure, is then linearly interpolated from the FM simulation results. Note that Equation 2.14 is derived for ordered spheres, but is expected to yield a reasonable estimation of the critical saturation for randomly distributed spheres. Note too that Equation 2.14 holds for a cubic domain, where all of the domain dimensions are equal.

Given the random distribution of spheres, it was necessary to ensure that the results are independent of the domain size. Figure 2.14, therefore, shows critical pressure calculated at an SVF of $\varepsilon = 0.16$, vs. N, the total number of spheres in the computational domain. At any given SVF, the number of spheres increases with the size of the domain; hence each N represents a certain domain size at a certain SVF. The results indicate that calculated critical pressure becomes reasonably independent of the domain size at $N = 27000$. If the spheres were orderly distributed, this would correspond to a domain of $30L_s \times 30L_s \times 30L_s$. Note that the numerical results for the critical pressure are independent of both the total thickness of the superhydrophobic coating and the computational domain thickness. Given the definition of critical saturation, which corresponds to the immersion of the first layer of

particles by water, the critical pressure does not depend on the total and computational domain thicknesses.

Because of the randomness of the geometry, it was also necessary to ensure that the results are reasonably repeatable. To this end, the domains were generated five times at each SVF, and the corresponding calculations were carried out for each of these domains. The results indicated that the calculations are reasonably repeatable at N = 27000, with a relative standard deviation of about 1%.

2.5.4 Extension of analytical method to randomly distributed spheres

Equation 2.7 is derived for a superhydrophobic coating with ordered particles, for which the SVF is homogeneous, because of the inherent symmetry of such coatings. In an actual coating with random particles, distribution of particles is heterogeneous; thus, one can define a local SVF. The minimum capillary force, and therefore the critical pressure, on the surface of a superhydrophobic coating correspond to the location with the lowest local SVF.

We used Equation 2.7, along with the minimum local SVF, to calculate the critical pressure of a superhydrophobic surface with randomly distributed particles. To calculate the local SVFs, we used the Voronoi method, following the work of Samaha *et al.*, (2011b) where Equation 2.3 was used, along with the maximum local gas area fraction, to calculate the critical pressure of a superhydrophobic surface with randomly distributed posts; a 2-D

Voronoi method was used to calculate the local gas area fractions. Here, we extended the same approach to our 3-D geometry, to calculate the local SVFs. To this end, we used the computational domains that were generated for our FM simulations, and we divided each domain into several volume elements. Each volume element was attributed to the closest particle in the domain, creating a 3-D cell around each particle. The volume of each cell, and the corresponding local SVF, was calculated. The minimum local SVF on the top face of the domain (i.e., the surface of the superhydrophobic coating), was then used in Equation 2.7 to calculate the critical pressure. For each case, the random domain was generated five times, and the Voronoi method was applied, to ensure that the calculations are repeatable. Figure 2.15 shows the local SVF contours on the top face, calculated for a domain of randomly distributed spheres with an overall SVF of 0.34. Each local SVF corresponds to one of the surface Voronoi cells. As can be seen, the local SVF fluctuates between 0.16 and 0.43. As expected, the overall SVF, 0.34 in this case, lies between the maximum and minimum local SVFs. The breakup happens at the cell with the minimum SVF.

We have compared predictions of our FM simulations for the randomly distributed spheres with our analytical method at different SVFs, as shown Figure 2.16. Note that ε represents the overall solid volume fraction. The minimum local solid volume fraction was used along with Equation 2.7 to calculate the analytical values. For comparison, the analytical and numerical results of the ordered spheres are shown here as well. Similar to what was observed for ordered spheres, the critical pressure of the superhydrophobic surface with

randomly distributed particles increases with the solid volume fraction, because the average gap between the spheres decreases as SVF increases. As can be seen, the analytical results calculated with the minimum local SVF are in reasonable agreement with the FM simulations. Comparison of the random and ordered sphere results indicates that superhydrophobic surfaces with randomly distributed particles possess lower corresponding critical pressures than their ordered counterparts. This is expected, because the maximum distance between the randomly distributed spheres is higher than that of the ordered spheres at the same SVF, allowing water to penetrate more easily thorough the porous area, and so the superhydrophobicity would vanish at a lower pressure.

Finally, we have compared our FM and our analytical calculations for superhydrophobic surfaces with randomly distributed granular particles for a range of particle diameters $10 < d_s < 100$ μm, at a constant SVF of $\varepsilon = 0.34$, as can be seen in Figure 2.17. The results indicate that the critical pressure decreases as the particle diameter increases. This is because the capillary radius increases with particle size, causing the menisci curvature and hence the surface tension forces to decrease.

2.6 Conclusions for Particle Coatings

In this chapter, a numerical method has been used to predict the critical pressure, the hydrostatic pressure above which a departure from the Cassie state is expected, for submerged superhydrophobic surfaces. Predictions of our numerical morphology-based

simulations have been compared with those of the analytical expression developed for surfaces made of microfabricated vertical posts (Zheng *et al.*, 2005), and reasonable agreement has been observed. Our simulations have then been used to quantitatively evaluate resistance of granular coating with three-dimensionally random microstructures where no analytical method is applicable. We have also developed a new analytical expression based on the balance of forces on the air–water interface to predict the critical pressure of superhydrophobic coatings consisting of ordered spherical objects. Good general agreement has also been observed between the results of our new analytical relationship and numerical simulations.

The numerical simulations reported in this paper indicate that for granular coatings with identical particle diameters, critical pressure increases with solid volume fraction. However, increasing particle diameter results in lower critical pressures when the coating's solid volume fraction is held constant.

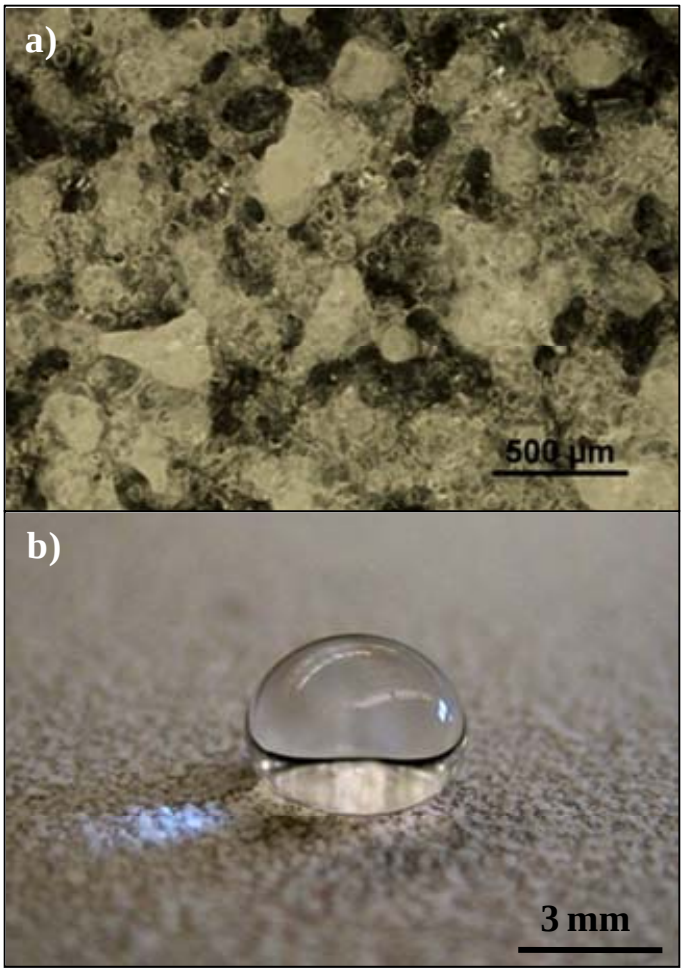

Figure 2.1: (a) an optical microscopic image of our aerogel superhydrophobic coating. (b) an image of a droplet deposited on our superhydrophobic surface showing a large contact angle.

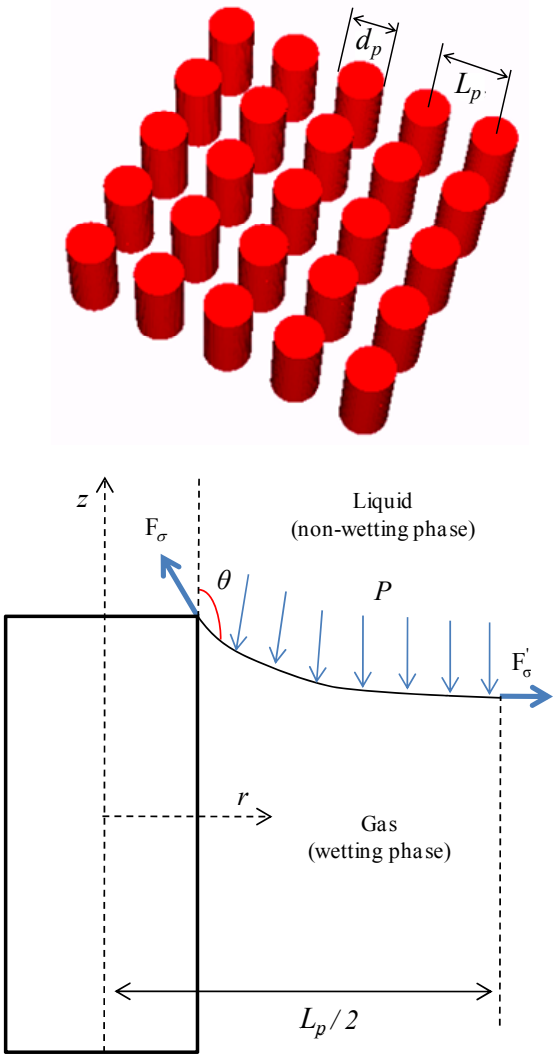

Figure 2.2: Schematic of an array of ordered posts and the force balance on the gas-liquid meniscus. Note that only half of the meniscus is shown, as the geometry is symmetrical.

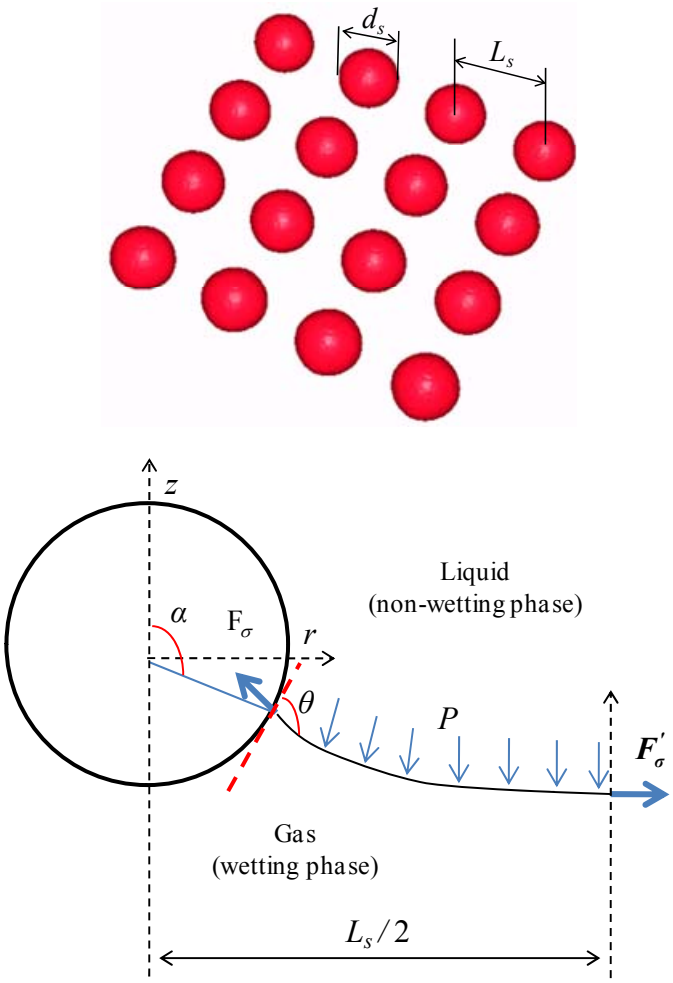

Figure 2.3: Schematic of an array of ordered spheres and the force balance on the gas-liquid meniscus. Note that only half of the meniscus is shown, as the geometry is symmetrical.

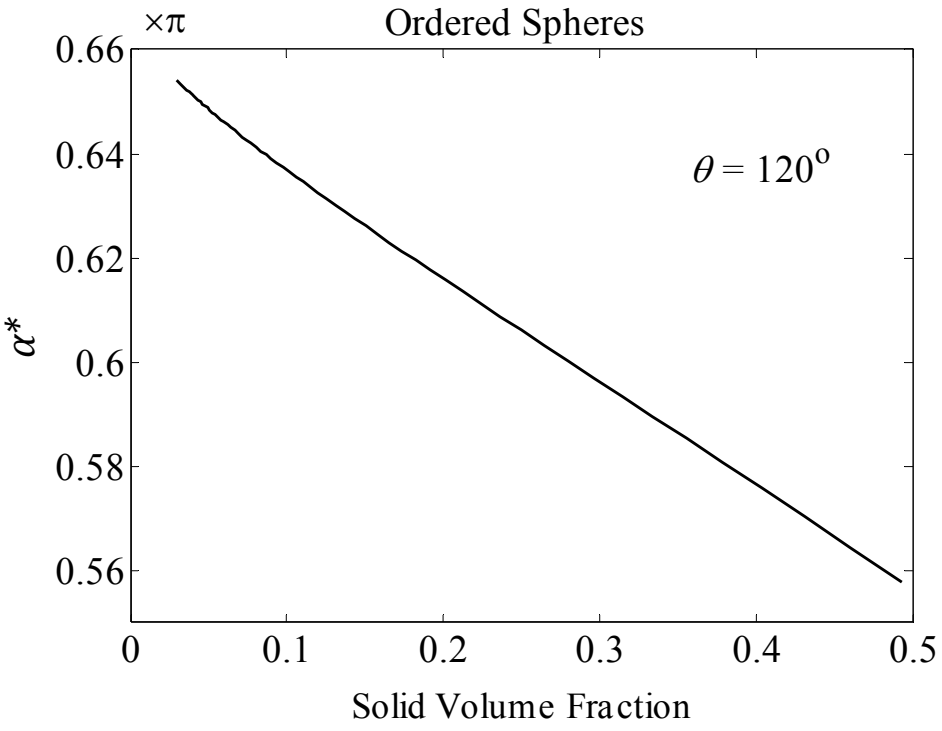

Figure 2.4: Critical angle α^* calculated by our analytical method at different solid volume fractions.

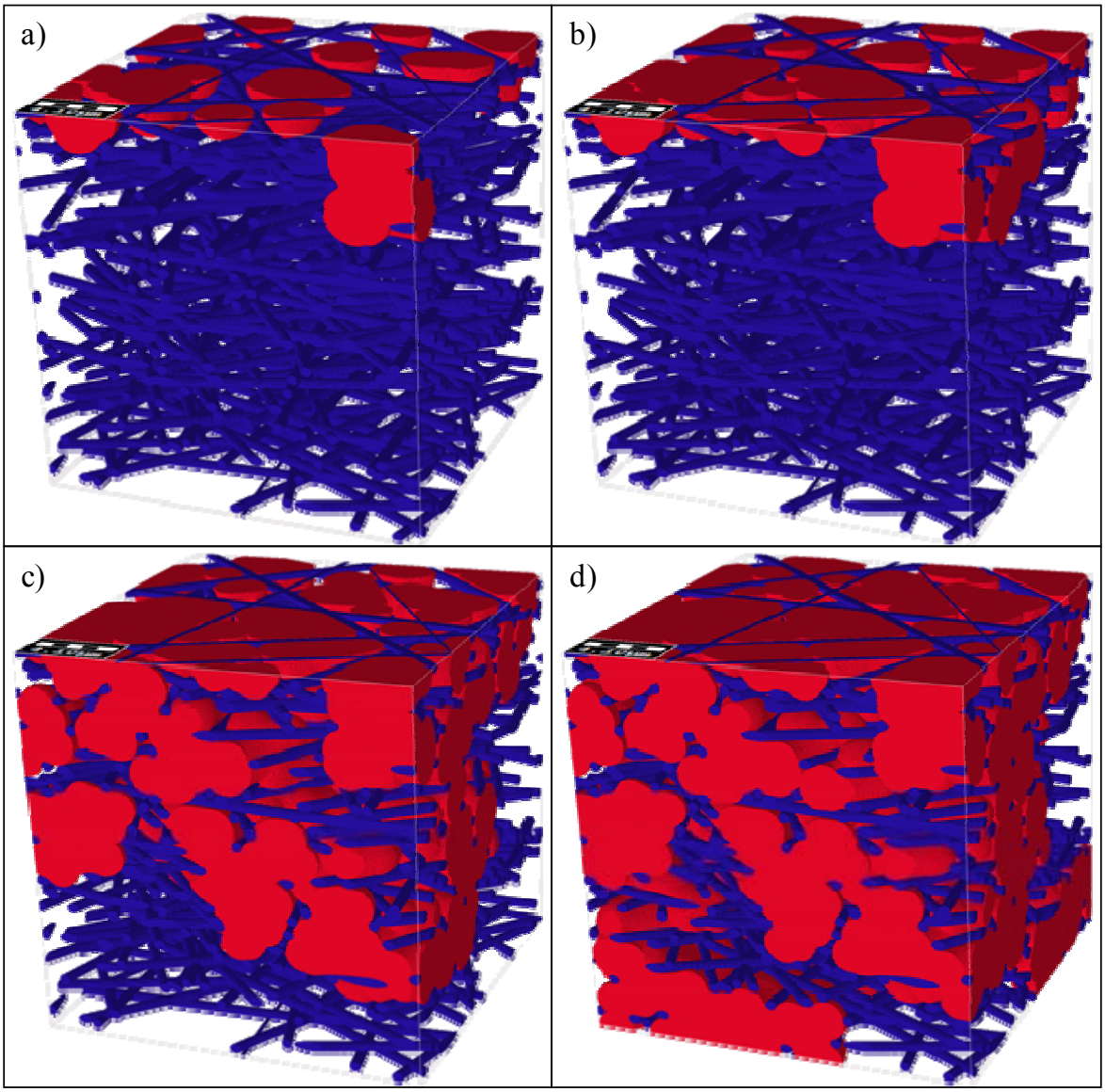

Figure 2.5: A visualization of different stages of water intrusion simulation into a unimodal fibrous structure with SVF of 10%, unimodal fiber diameter of 500 nm with random in-plane fiber orientation, using the Full-Morphology method. Corresponding pressures are: a) 58.983 kPa, b) 68.235 kPa, c) 77.333 kPa, and d) 80.930 kPa. The non-wetting fluid (water) represented in the red region is made up of spheres fitted into the domain.

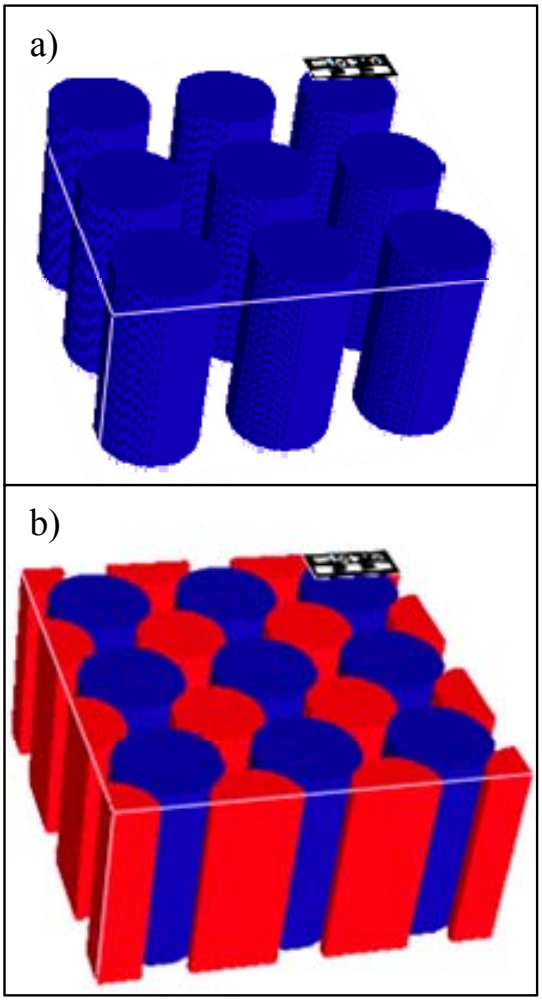

Figure 2.6: Full-morphology simulation of saturation for a surface with ordered posts of a hydrophobic material; ε = 0.46. Results at (a) p = 1750, and (b) p = 1775 Pa; blue corresponds to the posts and red corresponds to liquid.

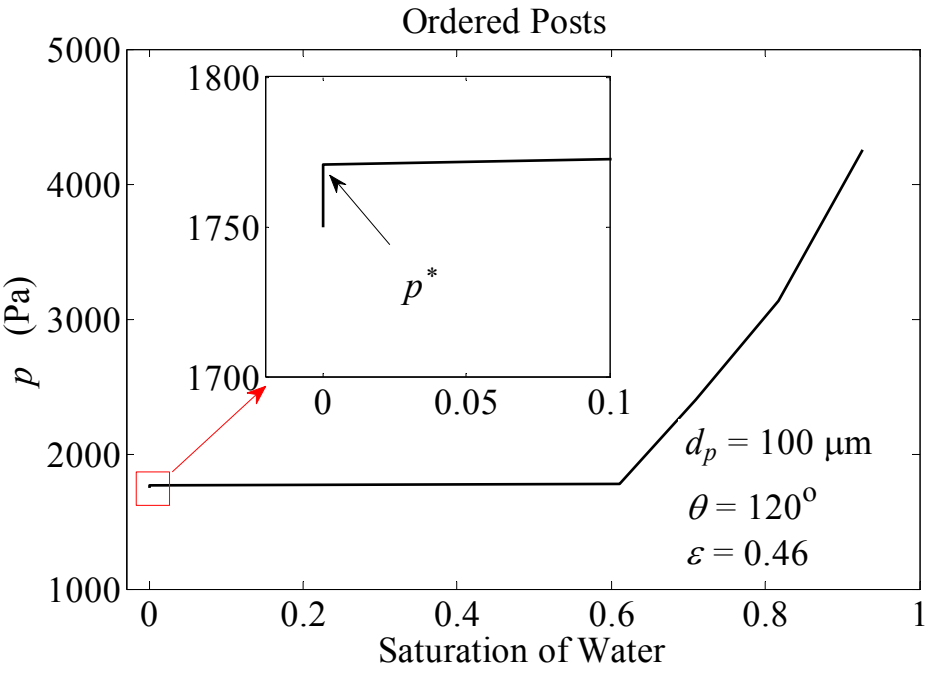

Figure 2.7: Full-morphology simulation results: pressure vs. saturation of water for the superhydrophobic surface with ordered posts; $\varepsilon = 0.46$.

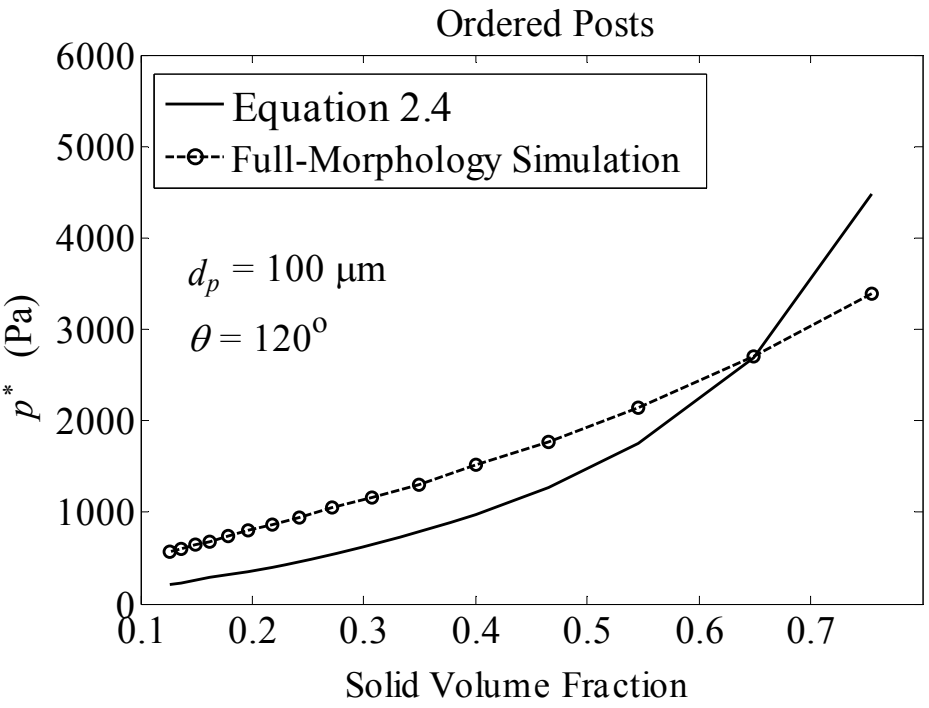

Figure 2.8: Comparison of the analytical and simulation results: critical pressure vs. solid volume fraction for the superhydrophobic surface with ordered posts.

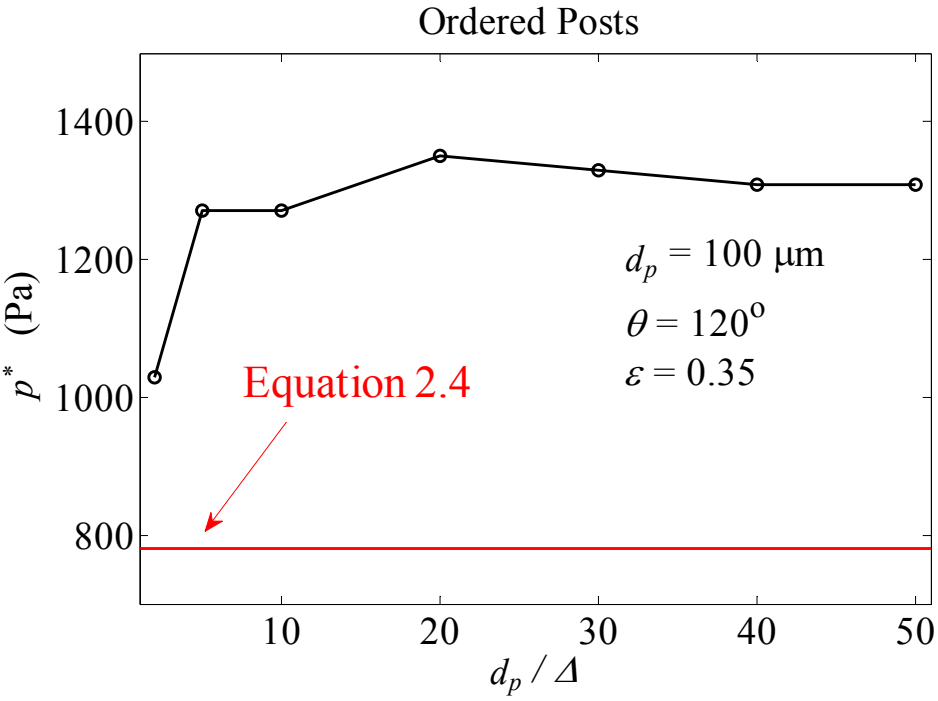

Figure 2.9: Critical pressure of the superhydrophobic surface with ordered posts, calculated by simulation at different voxel sizes; ε = 0.35.

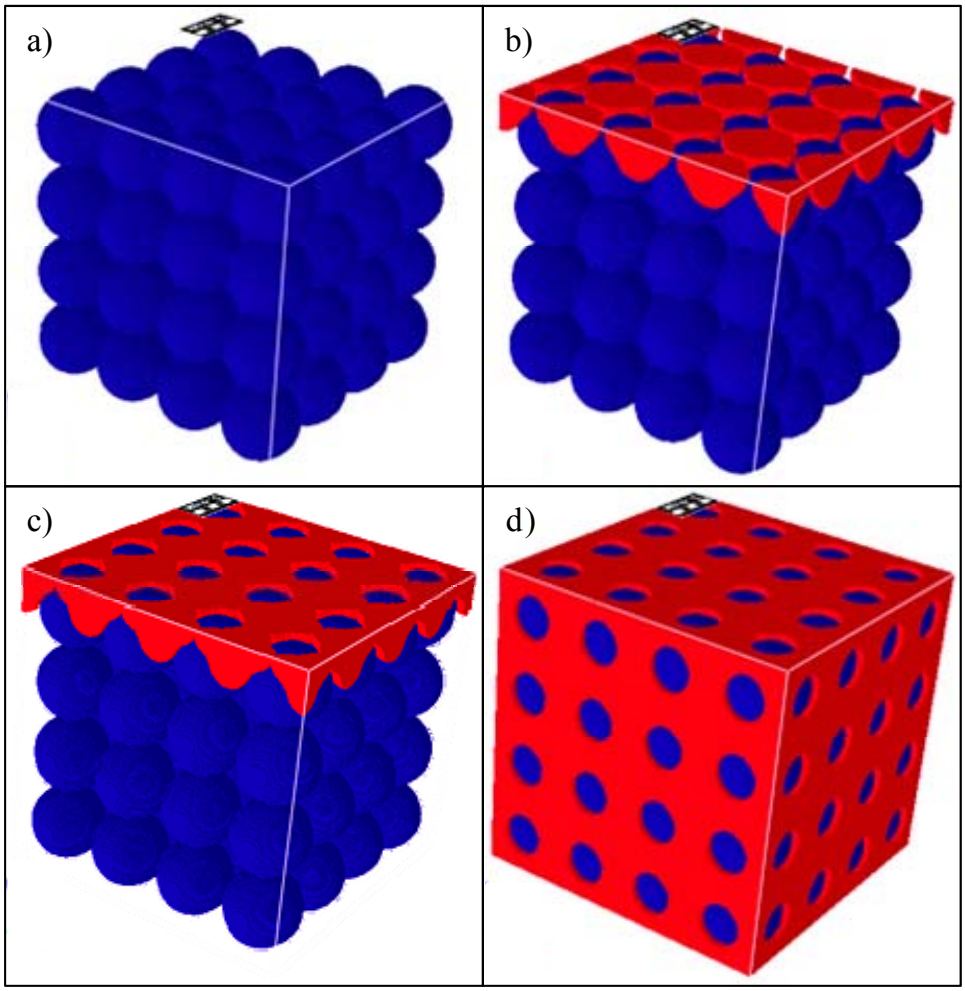

Figure 2.10: Full-morphology simulation of saturation for a surface with ordered spheres of a hydrophobic material; ε = 0.49. Results at (a) $p = 0$, (b) $p = 2500$, (c) $p = 3200$, and (d) $p = 3500$ Pa; blue corresponds to the spheres and red corresponds to water.

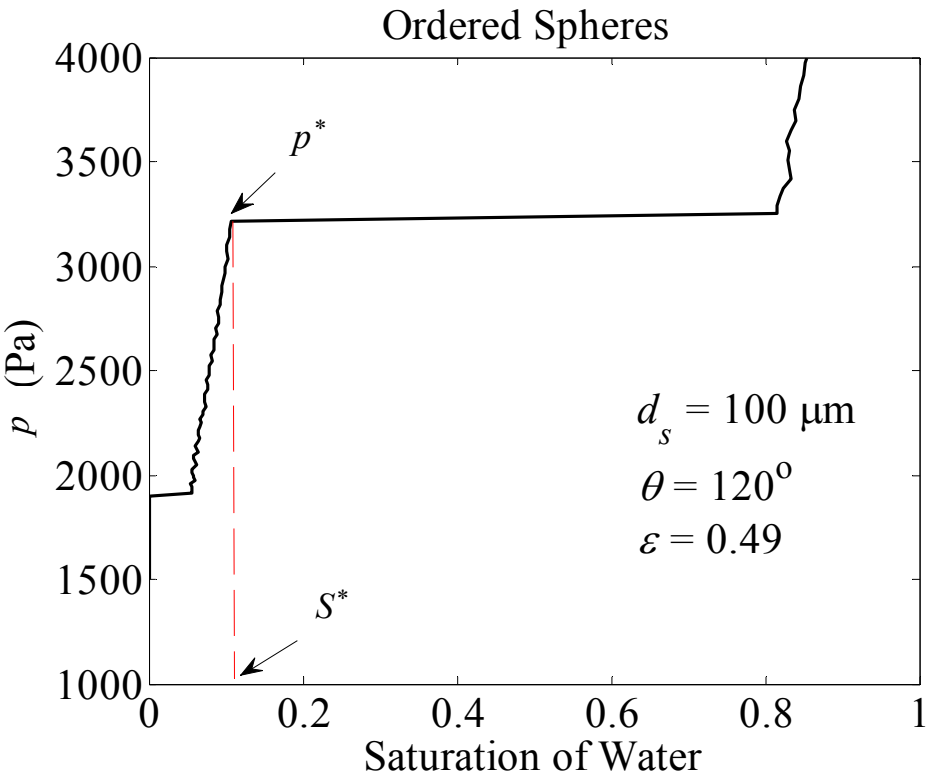

Figure 2.11: Full-morphology simulation results: pressure vs. saturation of water for the superhydrophobic surface with ordered spheres; $\varepsilon = 0.49$.

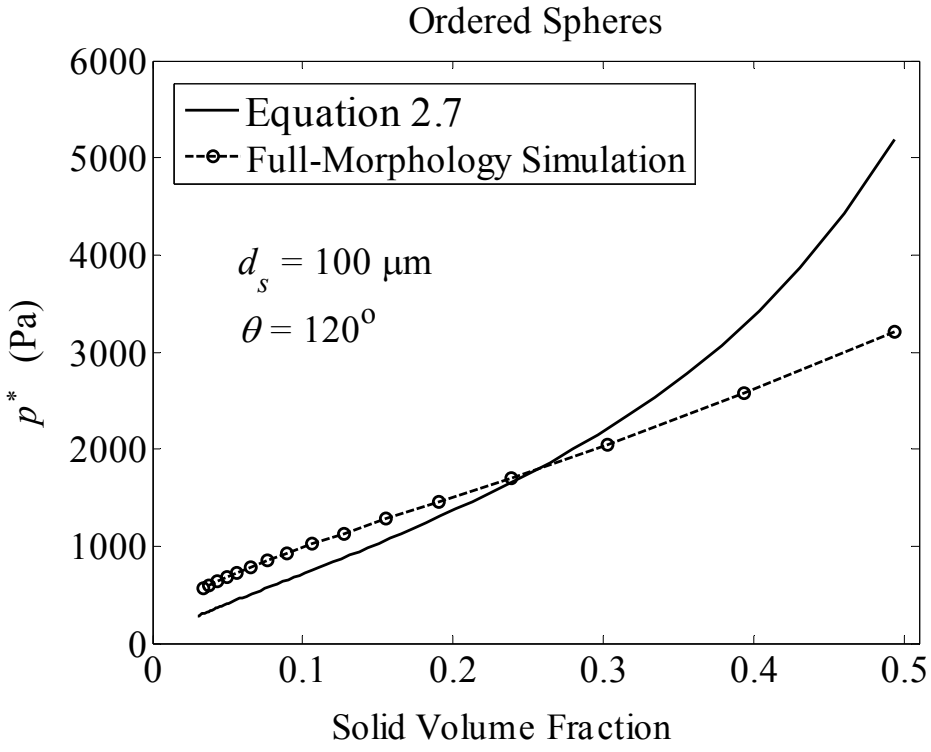

Figure 2.12: Comparison of the analytical and simulation results: critical pressure vs. solid volume fraction for the superhydrophobic surface with ordered spheres.

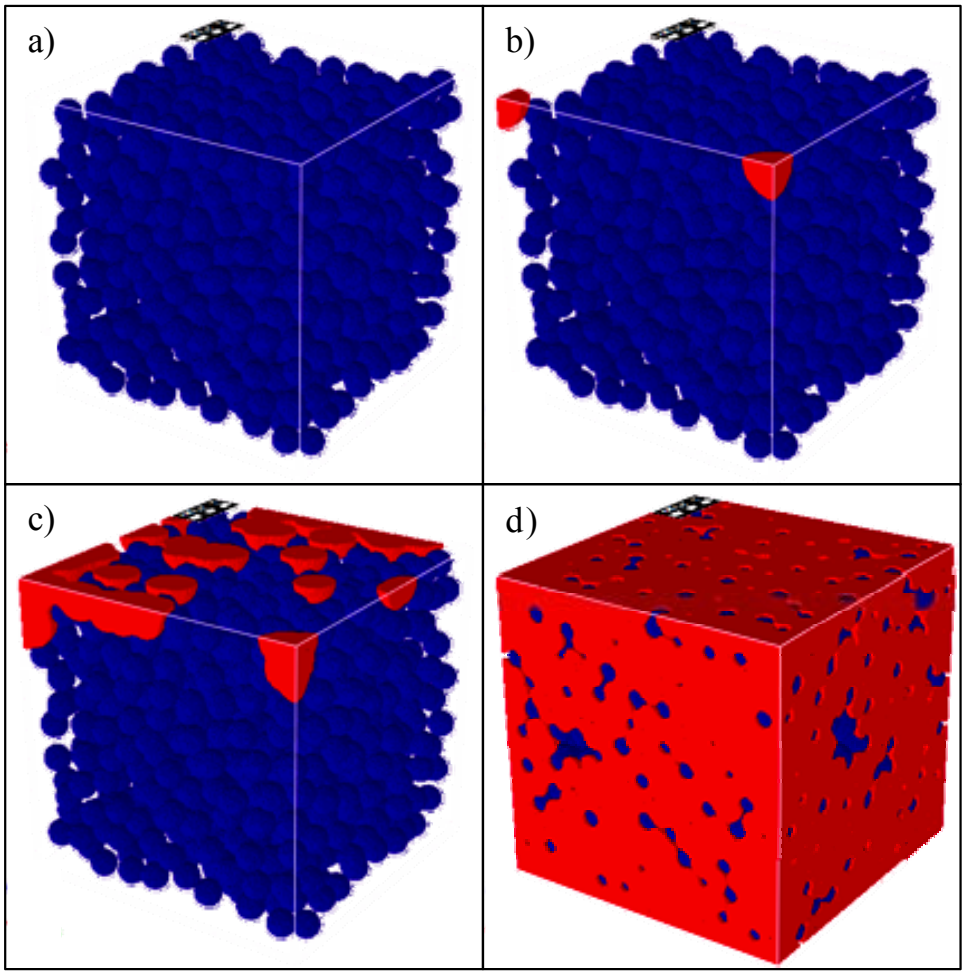

Figure 2.13: Full-morphology simulation of saturation for a surface with random spheres of a hydrophobic material; $\varepsilon = 0.34$. Results at (a) $p = 0$, (b) $p = 600$, (c) $p = 1000$, and (d) $p = 2000$ Pa; blue corresponds to the spheres and red corresponds to water.

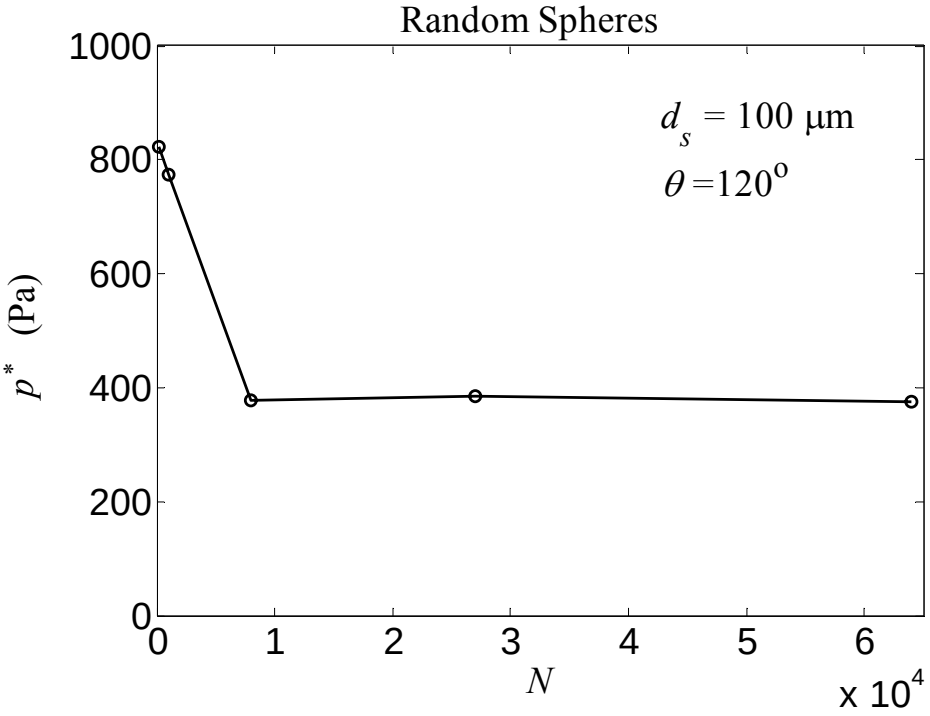

Figure 2.14: Normalized critical pressures of the superhydrophobic surface with randomly distributed spheres, calculated by simulation at different domain sizes; $\varepsilon = 0.16$.

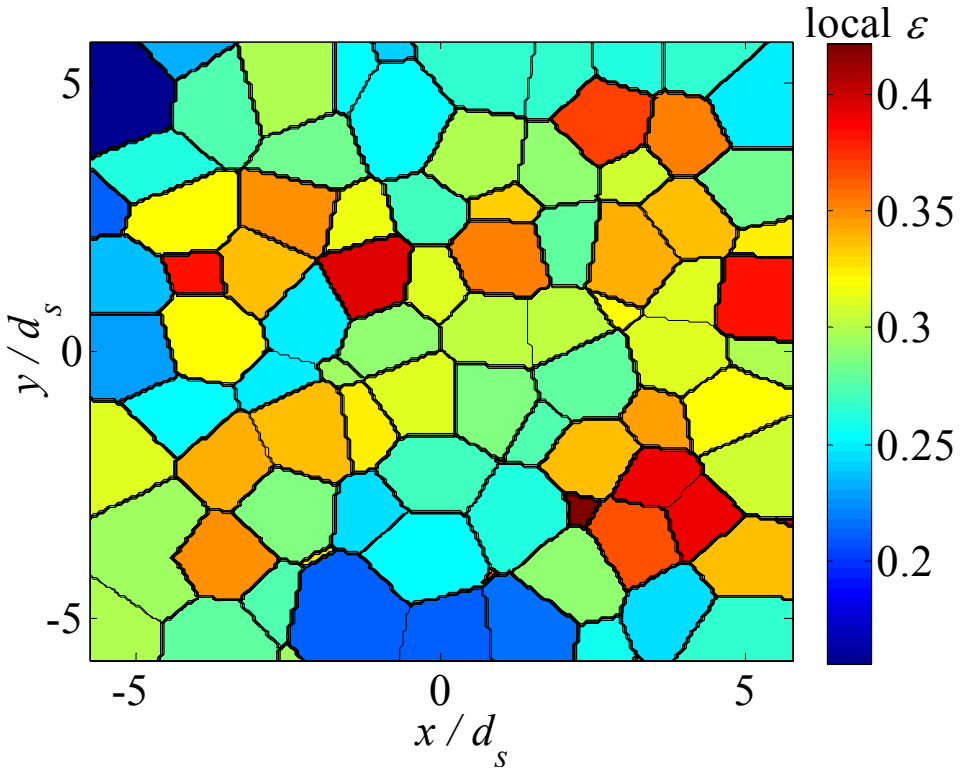

Figure 2.15: Local solid volume fraction contours on the top face of the domain, calculated using Voronoi method ; $\varepsilon = 0.34$.

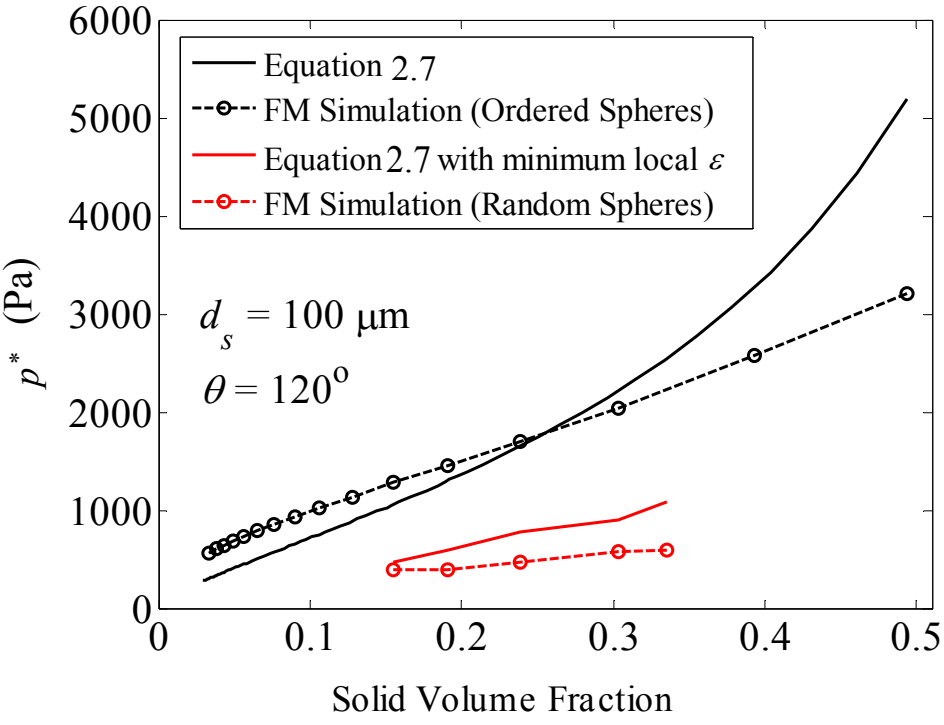

Figure 2.16: Comparison of the analytical and simulation results: critical pressure vs. solid volume fraction for the superhydrophobic surface with randomly distributed and ordered spheres.

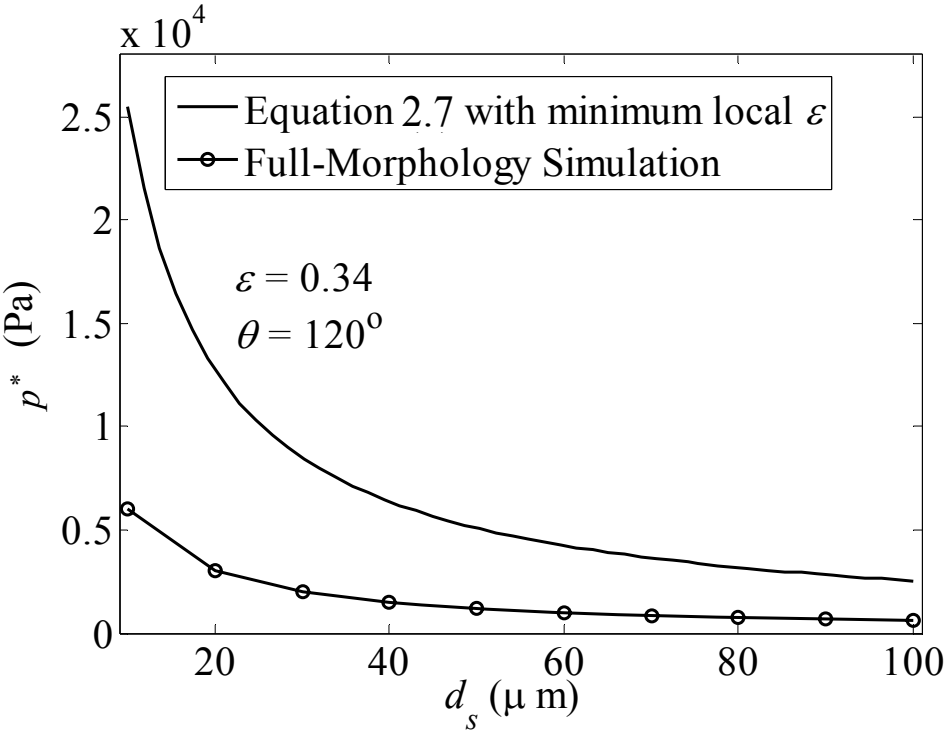

Figure 2.17: Comparison of the analytical and simulation results: critical pressure vs. sphere diameter for the superhydrophobic surface with randomly distributed particles; ε = 0.34.

CHAPTER 3 Modeling Resistance of Nanofibrous Superhydrophobic Coatings to Hydrostatic Pressures[5]

3.1 Overview

Recent studies have shown that superhydrophobic coatings can also be produced using polymeric nanofibers manufactured via electrospinning (Ma *et al.*, 2005 and 2008). Electrospinning is more cost effective than microfabrication, and can better conform to surfaces with arbitrary shapes. With electrospinning, however, one has less control over the coating microstructure. Different methods of electrospinning can produce fibrous coatings with varying degrees of order and controllability in how fibers are laid down. Nanofibers produced using DC electrospinning often have random in-plane orientations, owing to the unstable whipping of the polymer filament as it is released from the Taylor cone (Yarin *et al.*, 2001; Reneker and Yarin, 2008). Electrospinning using our AC method, described in the next section, reduces this instability, and can therefore produce fibers with a higher degree of order, allowing them to be stacked in layers orthogonal to one another (Sarkar, *et al.*, 2007; Kessick and Tepper, 2006; Leveit and Tepper, 2004; Kessick and Tepper, 2003 and 2004). To the authors' knowledge, superhydrophobic coatings produced via electrospinning have never been studied for their use in underwater applications, except

[5] The contents of this chapter is published in an article entitled "Modeling resistance of nanofibrous superhydrophobic coatings to hydrostatic pressures: the role of microstructure," by T.M. Bucher, B. Emami, H. Vahedi Tafreshi, M. Gad-el-hak, and G. Tepper, Physics of Fluids **24**, 022109 (2012).

for the work of others in our own group (Samaha *et al.*, 2011). Stability of the air–water menisci inside the pores of a superhydrophobic coating depends on the coating's microstructural parameters. These parameters include, but are not limited to, overall porosity, fiber diameters, fiber orientation, and, in the case of multi-component fibrous structures, difference in diameter and population representation of each component. To guide in the design and optimization of these coatings, for this chapter we design virtual 3-D fibrous superhydrophobic structures with different microstructural parameters, and virtually test their resistance against elevated pressures. This will be accomplished by using the Full-Morphology method described in Chapter 2, in which the occupied void volume between the disordered fibrous assemblies is measured during a virtual water intrusion simulation (Hazlett, 1995; Hilpert and Miller, 2001).

It is important to point out that the study presented in this chapter is focused on the importance of the microstructure of a fibrous superhydrophobic coating on its stability against hydrostatic pressures. Establishing such relationships between a coating's fibrous microstructure (e.g., porosity) and its drag reduction percentage is a major challenge that should be addressed in a separate study, in which an accurate prediction of the exact 3-D shape of the air–water interface is needed. For the latter, once the exact shape of the air–water interface is obtained, one can calculate the exact solid area in contact with water, the area causing friction due to the no-slip boundary, and predict the drag reduction percentage brought about by the coating.

What follows herein is a brief description of AC and DC electrospinning (Section 3.2), our modeling strategies for generating virtual 3-D fibrous microstructures (Section 3.3), and simulating water intrusion (Section 3.4). Inspired by the work of Zheng *et al.* (2005) for vertical microposts, we have developed analytical expressions like those in Chapter 2 for predicting critical pressure for in-plane, equally-spaced, parallel fibers (Section 3.4.1), and used it to better examine the accuracy of our geometry-based simulations against similar analytical expressions derived in the work of Tuteja *et al.* (2008). A comprehensive parametric study is then presented for bimodal coatings with random and orthogonal microstructures in Section 3.5. This is followed by our conclusions in Section 3.6.

3.2 Electrospun Nanofiber Coatings

In a typical electrospinning process, a DC electric field is applied to a polymer solution contained within a capillary needle. Such a field exerts a force on the polymer solution, distorting the fluid surface at the tip of the injection needle into a characteristic Taylor cone, caused by the balance between surface tension and the applied electric force. When the electric force on the liquid exceeds a critical limit, a jet of charged liquid emerges from the tip of the Taylor cone, and if the solution contains a polymer solute, continuous polymer nanofibers can be produced with diameters well below 1 μm. However, in a DC-electrospun fiber mat, the electrically charged fibrous output from the capillary needle swings and spirals wildly due to Coulombic self-repulsion, leading to loops in the deposited fiber diameters on the order of several millimeters. However, as the self-repulsion also occurs on a much smaller scale, these fiber loops contain smaller loops on

the micron order visible in the coating of polyethylene oxide fibers shown in Figure 3.1a. Tepper and his group have demonstrated a novel use of combined AC and DC potentials in the electrospinning process, resulting in reduction or elimination of the fiber whipping (Sarkar, *et al.*, 2007; Kessick and Tepper, 2006; Leveit and Tepper, 2004; Kessick and Tepper, 2003 and 2004). This allows one to better control the fiber lay-down process, and thus design coatings with engineered microstructures. In the DC-biased AC-electrospinning technique, an AC field is applied on top of the conventional DC potential, so that the charge polarity (positive/negative) on the fiber reverses at a frequency determined by the applied AC frequency and the fiber production/spinning rate. The DC bias maintains a net drawing force on the fiber, while the AC modulation in the charge polarity eliminates the instability caused by Coulombic self-repulsion. The result is a highly ordered medium such as that shown in Figure 3.1b.

A superhydrophobic coating comprised of electrospun nanofibers can potentially generate drag-reduction and pressure-tolerance performance characteristics similar to those of microfabricated posts and ridges, but at a much lower cost. To encourage the desired inter-fiber voids within the medium, one can produce coatings with bimodal fiber-diameter distributions. Generally speaking, the coarse fibers in such coatings help to provide the required porosity and thickness, whereas fine fibers control the pore size.

3.3 Virtual Fibrous Structures

To generate 3-D virtual models resembling the microstructure of an electrospun fibrous medium, we have developed a computer program to produce random and ordered fibrous structures with different fiber diameters, porosities, thicknesses, and orientations. To better mimic the planar microstructure of electrospun fiberwebs, no through-plane orientation has been considered for the fibers. Virtual fibrous structures are generated with random and orthogonal fiber orientations to emulate electrospun coatings obtained from DC and AC electrospinning, respectively. Note that material density of the electrospun fibers is assumed to be constant regardless of their diameters, as the choice of fiber density and its variations with diameter are of minor importance in our modeling.

Figure 3.2a depicts a virtual bimodal fibrous structure with a random in-plane fiber orientation. Note that the fibers are allowed to overlap and cross through each other. This is a simplification considered in our simulations with structures having random fiber orientations, which helps us circumvent some of the complexities involved in generating size-independent disordered fibrous domains, as reported in our previous publications (Maze *et al.*, 2007a and b). Allowing the fibers in each layer to cross through one another also helps us to better control the solid volume fraction (SVF) of the virtual coatings. Based on our previous experience with modeling transport properties of fibrous media, we believe that such a simplification has a negligible influence on the accuracy of the results and conclusions reported in this paper, especially when working with nanofibers (Tahir and Tafreshi, 2009; Hosseini and Tafreshi, 2010). It is important to note that SVF is an

implicit parameter in our coatings, representing the ratio of structure volume occupied by solid fibers to the total volume. The term is arrived upon differently for models representing DC- and AC-electrospun coatings. DC-spun fiber mats are composed of randomly deposited spiral fibers (filaments), as described in the previous section. Recall that in experiment, these fibers form curly filaments when deposited on a flat substrate, stacked on top of one another with loop diameters (i.e., length scales) varying from the order of microns to the order millimeters. Therefore, the simulation domain should be much larger than the length scale of the surface morphology, otherwise the SVF cannot be accurately predicted. Unfortunately, with current computational power, our simulation domains must be much smaller than the few millimeters that would be necessary to cover the entire range when the fibers are as small as 100 nm (i.e., electrospun fibers). Moreover, modeling such random curvatures and their effect on the system in intricate detail is, in general, a computational task beyond the scope of this work, and for the sake of simplicity, we model the fibers as straight cylinders and allow them to interpenetrate, so that a desired SVF can be achieved on the scale of our simulations when modeling DC-electrospun fibrous structures. Experimentally, there is no way of knowing the SVF of a DC-spun fiber-mat prior to production. This is because of the complicated loops and curves the fibers form, leading to a non-linear increase in the coating's thickness with time (time being proportional, but not necessarily linearly, to deposited mass). Therefore, the only way one can know the SVF of a DC-spun coating is by characterizing its physical properties (e.g., weight per unit area, thickness …) after the coating is made. In our model, once a fibrous structure is generated, its volume is descretized into voxels, and the voxels

can only be filled (solid fiber) or empty (air or water). The SVF is the ratio of the solid voxels to the total number of voxels, so there is no double-counting of the volume of overlapping cylinders. Because fibers are allowed to overlap and assume orientations askew to the domain boundaries, changes in SVF are more incremental as fibers are added. This allows the virtual DC structures to be generated with an input SVF upon which to target.

In the case of orthogonal fibrous structures, which emulate coatings produced using the AC method, the fibers in a given layer all face either the *x*- or *y*-direction. What one could consider to be the smallest divisible "unit layer" in a given sample of these structures would be two layers of fine fibers, and two layers of coarse fibers. Note that any given layer only consists of only one type of fiber. As one has better control over a coating's microstructure with AC electrospinning, we separate the coarse and fine fibers into distinct layers in our orthogonal structures. In the interest of encouraging the first layer of the coating to act as the bottleneck for water intrusion, with fiber spacing as constrictive as reasonably achievable, the outermost pair of layers in our orthogonal coatings is comprised of fine fibers. Since the fibers in each layer are parallel to each other, there are no concerns with fibers crossing through one another as there were for the random structures. As can be seen in Figure 3.2b, fibers in adjacent layers lie over and under those of their neighboring layers without interpenetrating, as one should expect. Here SVF does not have to be an input, unlike the case for mats with overlapping fibers. In this case, SVF is an output of our

structure generation algorithm based on fiber population and spacing, which is, of course, more realistic insofar as how one would estimate the SVF for a given fabricated coating.

In Figure 3.2b, note also the semi-random placement of fibers within a layer. It is assumed that the AC electrospinning technique, while maintaining significantly high order in its layers, will not achieve perfect fiber spacing across a given layer. Therefore, we have decided to introduce an arbitrary degree of "noise" into an otherwise perfectly spaced structure, by allowing some limited randomness in fiber placement, while still restricting any fiber overlap. For a given fiber, the maximum random distance δ it can be placed from its even-spacing position is determined by

$$\delta = \min\left(\frac{(s/n) - d}{2},\ \eta d \right) \tag{3.1}$$

where s represents the in-plane size of the computational domain, n is equal to the number of fibers in the layer, and d represents fiber diameter (subscript c or f for coarse or fine fibers, respectively). The term η is equal to 3.5 for coarse fibers, and 1.72 for fine fibers, and is applied as an upper arbitrary, but educated, limit on the magnitude of δ. This upper limit is imposed in order to avoid generating virtual coatings with excessive non-homogeneity, which can lead to unnecessary statistical uncertainty in our simulation results. These values correspond to the maximum spacing deviation in fiber placement in a structure with an SVF of 11.2%, a fine fiber diameter of 100 nm, a coarse fiber diameter of 500 nm, and coarse-fiber number fraction of 0.1, in which case adjacent fibers in a layer

would be able to touch, but not overlap. Any structure whose coarse and/or fine solutions to Equation 3.1 are greater than those prescribed for this given structure will be assigned the upper-limit value for their respective δ.

The relation between coarse or fine mass fraction m_c or m_f and their respective number fraction in a bimodal 3-D fibrous structure is given as (for more details see Tafreshi *et al.*, 2009):

$$m_c = \frac{n_c d_c^2}{n_c d_c^2 + n_f d_f^2} \tag{3.2a}$$

$$m_f = \frac{n_f d_f^2}{n_c d_c^2 + n_f d_f^2} \tag{3.2b}$$

where n_f and n_c are, respectively, the number fraction of fine and coarse fibers, and d_c and d_f are coarse and fine fiber diameters. While mass fraction is a more practical representation experimentally, number fraction is a more convenient input for our simulations, especially for the orthogonal structures, which are constructed based on number of fibers. Nevertheless, one can be estimated from the other in most cases. In the case of the orthogonal structures produced via AC electrospinning, number fraction can be determined using the rotational and translation speeds of the collector drum and polymer throughput, due to the controllability of fiber placement.

3.4 Critical Pressure Modeling and Validation

Capillary pressure of a hydrophobic porous material can be used to characterize its resistance against water intrusion. Previous works have shown that the relationship between capillary pressure and a medium's saturation is dependent on the size distribution of the medium's void spaces (Jaganathan *et al.*, 2008 and 2009). By increasing the hydrostatic pressure of water in which an air-filled hydrophobic material is submerged, water is able to pass into more constrictive spaces within the medium, thereby reducing the wetting-phase saturation. As the fluid interface boundary fully passes inside the coating, its superhydrophobicity diminishes, and thus its effectiveness is compromised.

In general, the required pressure for penetration of a non-wetting fluid into a porous medium filled with a wetting fluid is governed by the Young–Laplace equation, stated again here for convenience:

$$p_c = -\frac{2\sigma\cos\theta}{r} \tag{3.3}$$

where p_c represents capillary pressure, σ is the surface tension between water and air, θ represents the contact angle of the non-wetting phase (in this case, water) on a flat sheet made of the same material as the fibers, taken arbitrarily to be 120 degrees for the simulations reported in this study, and r is the capillary radius. Higher pressure allows the water to penetrate through more constrictive void spaces, displacing the wetting fluid. As with our study on granular coatings, we used the Full-Morphology (FM) method, implemented using the GeoDict code described in Section 2.4, to perform our numerical

study. The FM method is a voxel-based approach. A voxel is the smallest unit of resolution within a given simulation domain (like a three-dimensional pixel), and is recognized as being fully occupied by one of three possible domain constituents: a solid fiber (blue in Figure 2.5), wetting phase (clear in Figure 2.5), or non-wetting phase (overlying red spheres in Figure 2.5).

It is important here to emphasize that the focus of the model in this chapter is on predicting the capillary pressure required to force water to penetrate into a hydrophobic fibrous structure, rather than investigating the exact shape of the air–water interface. Predicting the exact shape of the air–water interface requires a different modeling technique such as that of Lobaton and Salamon (2007), and Pzrikidis (2010), based on the constant-mean-curvature concept, which is difficult to apply to 3-D disordered fibrous surfaces. The FM method is an approximate method, but yet the only method that can be used with 3-D disordered fibrous structures with affordable computational requirement. To determine the accuracy of the FM method, we compare the FM results against analytical methods (see the next section).

3.4.1 Force-Balance Analysis for Ordered Parallel Horizontal Fibers

In this section, we present a force balance analysis to better examine the accuracy of our FM simulations, and to provide a comparison between the morphology-based and physics-based predictions. The force balance method was first presented by Zheng *et al.* (2005) and

later by Lee and Kim (2009), for characterizing superhydrophobic surfaces made up of microfabricated vertical posts. These authors used a balance of forces to illustrate the interplay between the physical mechanisms that promote or inhibit meniscus instability. The balance of forces can be tailored to apply to a meniscus formed between parallel horizontal cylinders. This problem is slightly more complicated than the problem of vertical posts, as the cross-sectional area in the through-plane direction is not constant. We consider a unit cell for a domain in which parallel cylinders are stacked in the thickness direction, with no space between the cylinders above and below. Thus, the balance of forces for pressure, illustrated in Figure 4a, is expressed as

$$p_{FB} = \frac{\sigma \cos((3\pi/2) - \theta - \alpha)}{L_c/2 - r_c \sin\alpha} \tag{3.4}$$

where L_c is the pitch or center-to-center distance between parallel cylinders, α represents the angle made by the solid contact point of the meniscus with the peak of the surrounding cylinders, and r_c is the radius of a cylinder. Critical pressure is determined by differentiating Equation 3.4 with respect to α , and setting this derivative equal to zero. Equation 3.4 only represents critical pressure when the general α has the specific critical value α^*, which is determined numerically. Note that α^* is the value for α that maximizes the pressure. Therefore, with the pitch defined in terms of SVF ($L_c = \pi r_c/(2\varepsilon)$ $L_c = \pi r_c / (2\varepsilon)$, where, recall, ε represents SVF), one obtains

$$p_{FB}^* = \frac{\sigma \cos((3\pi/2) - \theta - \alpha^*)}{r_c(\pi/(4\varepsilon) - \sin\alpha^*)} \tag{3.5}$$

The FM method uses Equation 3.3 to base the critical pressure threshold on the sphere with critical radius $r^* = L_c / 2 - r_c$ to fit precisely between two fibers (see Figure 3.3b). Substituting into Equation 3.3 yields

$$p_{FM}^* = -\frac{2\sigma \cos\theta}{r_c(\pi/(4\varepsilon) - 1)} \tag{3.6}$$

Figure 3.3c shows α^* as a function of SVF for three different contact angles. It can be seen that α^*, the equilibrium position of the air–water interface just before breakup, decreases with increasing contact angle. This indicates that the interface breaks up at a location deeper inside the fibrous coating if the contact angle is lower. Figure 3.3c also shows that α^* increases by decreasing SVF of the coatings, which again indicates that the interface breakup takes place deeper inside the fibrous structure when the SVF is lower.

Tuteja *et al.* (2008) developed an analytical model for superhydrophobic electrospun fiber mats, in which the fibers were considered to be parallel with one another and laid horizontally on a flat surface (one layer only) with a given fiber-to-fiber spacing. These authors applied the balance of forces for their geometry to produce two design criteria: "robustness angle" T^* and "robustness height" H^*. The critical pressures associated with the robustness angle and robustness height are shown with p_θ^* and p_H^*, where p_θ^* is the pressure required to force an interface sagging angle equal to that of the equilibrium contact angle between the interface and solid wall (fibers), and p_H^* is the pressure required for deflecting the air–water interface such that it dips into the pore space between two parallel fibers deep enough to touch the bottom flat surface:

$$p_{\theta}^{*} = \frac{\sigma \sin\theta}{r^{*}} \tag{3.7}$$

and

$$p_{H}^{*} = \frac{2\sigma(1-\cos\theta)r_c}{r^{*2}} \tag{3.8}$$

Figure 3.4a displays the critical pressure using each of the above four methods for a given fiber diameter and fluid contact angle as a function of SVF in a range relevant to electrospun fiber mats (1 to 20 %). It can be seen that good agreement exists between the predictions of the Full-Morphology (FM) p_{FM}^{*}, Force Balance (FB) p_{FB}^{*}, and the robustness angle p_{θ}^{*} equations, whereas the robustness height p_{H}^{*} follows a different trend from the other relations.

To better investigate the behavior of the above four models, we calculated $R_{FM}^{*} = p_{FM}^{*} / p_{FB}^{*}$, $R_{\theta}^{*} = p_{\theta}^{*} / p_{FB}^{*}$, and $R_{H}^{*} = p_{H}^{*} / p_{FB}^{*}$ and plotted them in Figure 3.4b–f versus contact angle and SVF. The prediction of our force balance approach has been chosen as the reference for comparing the above models with one another, as it does not have any of the restricting assumptions that have been considered in the other models discussed here, and so is expected to be the most accurate among them all. Figure 3.4b compares R_{FM}^{*}, R_{θ}^{*}, and R_{H}^{*} with one another when the contact angle is held constant at 120 degrees, but the SVF is varied, whereas Figure 3.4c provides a similar comparison when the contact angle is varied, but the SVF is held constant at 10%. From Figures 3.4b and 3.4c, one can conclude

that robustness height under-predicts the actual critical pressure, until SVF approaches the neighborhood of 18%, beyond which it over-predicts critical pressure; the FM method is accurate only when the contact angle is around 120 degrees; and the robustness angle method performs reasonably well when compared to the force balance method. To further study the degree of deviation of the FM, robustness angle, and robustness height methods from our general force balance method when SVF and contact angle are varied, surface contour plots of R^*_{FM}, R^*_{θ}, and R^*_{H} are shown in Figures 3.4d, 3.4e and 3.4f, respectively. As can be seen in Figure 3.4d, R^*_{FM} deviates quite significantly from the predictions of our general force balance method when the equilibrium contact angle is varied in a relevant range of hydrophobic surfaces (e.g., 90–140 degrees). However, changing SVF does not seem to affect the predictions of the FM method, indicating that when the error associated with the FM method is determined for a given contact angle and SVF, one can confidently use this method with other SVFs as long as the material of the fibers (and, of course, the fluid) is not changed. The robustness angle method seems to perform acceptably well with regards to variations in contact angle and SVF (see Figure 3.4e). The robustness height method seems to be least sensitive to variations in contact angle. However, this method consistently under-predicts critical pressure in the typical range of SVF for fibrous materials. As mentioned before, predictions of the robustness height method seem to be accurate only if the SVF is in the neighborhood of 18%, and over-predict critical pressure thereafter. The inaccuracy in the predictions of the robustness height model is believed to originate from the model's underlying assumption that a critical pressure is reached when the interface dips into the pore between two parallel fibers deeply enough to touch a

bottom horizontal surface directly beneath those fibers. In other words, a stable air–water interface can exist even when the meniscus is deflected beyond what would be considered the bottom surface in the robustness height model. It can be expected that as the SVF increases (fibers are closer together), the deflection of the meniscus becomes less significant, and the robustness height model approaches agreement with the other models. Beyond ~18%, the meniscus would fail due to the force balance before sufficiently deflecting to touch any bottom surface, hence the over-prediction of robustness height. It is also worth noting that in calculating the hydrostatic force exerted on the air–water interface, Tuteja *et al.* (2008) used the minimum gap between the surfaces of the two fibers $2r^*$, instead of the distance between the fiber surfaces at the location where the interface is in contact with the fibers. This simplification can also affect the model's prediction, especially at high SVFs.

Beyond the simple case of parallel fibers with ordered in-plane arrangements (or vertical posts), no analytical method is available to predict the exact pressure at which the air–water interface failure takes place, leading to the departure of the surface from the Cassie state. Exact predictions of critical pressure require accurate predictions of the exact 3-D shape of the air–water interface over a superhydrophobic surface. The FM method (purely geometric in nature) is a powerful, yet approximate, method that can be employed for studying the role of microstructure on the resistance of a superhydrophobic surface with disordered 3-D fibrous structures against elevated pressures. This is especially true if the objective of the study is investigating the influence of each individual microstructural

parameter on critical pressure, rather than the absolute values of the critical pressure itself, or the exact shape of the air–water interface. As mentioned earlier, our group has recently developed a methodology for predicting the exact 3-D shape of the air–water interface over superhydrophobic surfaces (Emami *et al.*, 2011). Our current interface tracking algorithm, however, is only applicable to surfaces made up of vertical posts.

3.4.2 Full-Morphology Simulation in Disordered 3-D Fibrous Coatings

Capillary pressure in a disordered fibrous coating is a function of microstructural parameters of a fibrous coating as follows:

$$p_c = f\left(\varepsilon, d_f, R_{cf}, n_c, t, \theta\right) \tag{3.9}$$

where R_{cf} is the diameter ratio between coarse and fine fibers, and t is the coating thickness. Pressure dependence on the right-hand side of Equation 3.9 is examined in more detail in the following two subsections.

For the simulations conducted in domains with disordered fibrous structures, special care should be taken to ensure that the volume considered for the simulations is large enough to statistically represent a real fibrous coating, especially in the *x*- and *y*-directions, where symmetry boundary conditions are applied. Note that mirror-like symmetry boundary conditions (Neumann) are used in our FM simulations, with the constraint that the center of a sphere along a boundary must be inside the domain. To eliminate any artifact that can be caused by the choice of symmetry boundary condition, one should consider simulation domains as large as computationally possible, or until no edge effect can be detected in the

simulation results (Hosseini *et al.*, 2010; Ashari and Tafreshi, 2009). It should also be noted that for a specific domain size and SVF, the finer the fiber diameter, the higher the population of the fibers in the simulation domain. Increasing the population of the fibers improves the statistical reliability of the results. Nevertheless, with finite computational power, any simulations for a given set of parameters has to be repeated on an ensemble of different structures, statistically identical in terms of their structural properties (SVF, fiber diameter…), to ensure confidence and relevance in the data. The results presented in this chapter are averaged over an ensemble of no less than five structures.

Figure 3.5 shows a series of capillary pressure–saturation curves for a statistical ensemble of randomly oriented bimodal fibrous coatings with an SVF of 10%, coarse and fine fiber diameters of 500 nm and 100 nm, respectively, and a coarse-fiber number fraction of 0.1. The trend observed in these curves is typical of such relationships in most porous media. At $p_c = 0$ (atmospheric pressure), the coating is fully saturated with air, or $S = 1$. As pressure is incrementally increased, water begins to penetrate, reducing the wetting-phase (air) saturation, but only as far as the most constrictive spaces in the coating for that given pressure allow (Equation 3.3). As pressure is further raised, the limiting pore size for intrusion becomes smaller, and water penetrates further into the coating. Eventually, pressure is sufficiently high such that the majority of the inter-fiber spaces can no longer constrict intrusion. Thus, saturation suddenly shifts to a lower value. From here, wetting-phase saturation approaches zero asymptotically with rising pressure, as water works its way into the smallest of the remaining pockets. Figures 3.5a and 3.5b illustrate the effect

of the size of the simulation domain for cubical structures varying by side length s. Figure 3.5b is a magnification of the region in Figure 3.5a in which coating failure is expected. As can be seen in Figure 3.5b, for a statistically homogeneous structure with constant microstructural parameters within the range of our study, predicted capillary pressure values are independent of domain size beyond a cubic side length of s = 10 μm. A side length of 24 μm is considered for the simulations reported in the next section (with the exception of our thickness dependence study presented in association with Figure 3.7), to further minimize statistical errors.

Also of great importance for conducting FM simulations free of artifacts is that the resolution of the domains is adequate such that the spheres' interactions with the domain are not obscured by a poor choice of voxel size. In this regard, a group of fibrous structures was constructed with dimensions and parameters such that the exact same structure was built with five different voxel resolutions, with fine fiber diameter acting as the size reference. Figures 3.5c and 3.5d illustrate the results of this voxel-size test (3.5d is a magnification of 3.5c), with dependence negligible at voxel sizes of 0.33-D_f or less. For the simulation results presented in this chapter, we used a characteristic voxel length of 0.2-D_f.

3.5 Results and Discussion

In this section, we study the effects of various microstructural parameters of our bimodal fibrous coatings on their pressure tolerance. Table 3.1 comprises a list of default microstructure parameters for coatings with random and orthogonal fiber orientations

(parameters not being varied for study will possess the values shown in the table). Predictions for structures modeled after DC-electrospun fibers and those for the AC method are divided out for ease of presentation.

Before elaborating on the results of our numerical simulations, it is important to establish a lucid definition for critical pressure, or failure pressure, in the context of our simulation method. To the knowledge of the authors, there is no universal definition for critical pressure—the pressure above which the surface starts to depart from the Cassie state (whether or not it reaches the Wenzel state). Note that drag reduction due to superhydrophobicity is the result of water being in contact with a reduced solid surface area. We assume that drag reduction begins to diminish when water penetrates deep into the coating such that the first layer of the fibers is in the liquid phase. When this happens, the fibers in the first layer act like external objects resisting against flow. Figure 3.6 is an FM simulation of an oversimplified geometry to illustrate the above concept. Notice in Figures 3.6a and 3.6b that while the menisci dip between the fibers of the first layer, the air–water interface still passes above these fibers, with Figure 3.6b being the threshold for critical pressure. Beyond the critical pressure (Figure 3.6c), the first layer is submerged, and the coating's drag reduction is diminished. Obviously, there is a possibility (especially for surfaces with random microstructures) that, due to non-uniformity in the coating's thickness, a stable air–water interface prevails, even if the interface is actually more than one fiber diameter into the material in some local areas. Thus, we define critical pressure

based on the average water saturation over the entire coating corresponding to the value obtained by assuming that water is penetrated one fiber diameter deep into the medium.

Figures 3.7a and 3.7b illustrate a direct comparison between the performance of structures varying only in the orientation of their fibers, as well as their respective dependence on coating thickness. Note that the range of thickness considered for this study allows the domain size in the z-direction to be less than the constraint of s = 10 μm stated in association with Figure 3.5. However, the dimensions in the x- and y- directions are held constant at 24 μm while the z-direction is varied. As a result, the population and size distribution of the inter-fiber spaces in a given layer are not affected by the structure simply having fewer layers. The resulting curves are therefore free of the distortions characteristic of inadequate domain size that are visible in Figures 3.7a and 3.7b. For Figure 3.7a, the fibers are laid orthogonally. The high degree of order is reflected in the stepwise progression of fluid penetration, with critical pressure relatively independent of thickness. The pressure at which that first layer becomes submerged is the same for all the coatings shown. This is because the size of the spacing between the fibers does not vary significantly from one layer to the next, thus the first layer of fine fibers becomes the bottleneck for the coating. The difference in saturation for each curve is due to the first layer of a coating comprising different percentages of the domain for varying thickness. The stepwise fluid intrusion also allows for visual identification on the curve for the description applied in the above paragraph for critical pressure.

Figure 3.7b displays the capillary pressure–saturation relationship for coatings in which the fibers are randomly oriented. The broader size distribution of the void spaces in the case of randomly laid fibers attributes to the shape of the curves in Figure 3.7b, depicting a smooth, continuous intrusion process as pressure rises, as was observed in Figure 3.5. A much greater dependence on thickness is also observed for capillary pressure in general, with dependence disappearing when the coating thickness is 24 μm or more, as the respective curves begin to fall on top of one another. Beyond this thickness, we can assume the coating to be homogeneous in the thickness direction for the microstructural parameters considered. As mentioned earlier, we establish our critical pressure definition for random fibers as being the pressure at which the first layer of fibers becomes submerged in water. In our simulations, we first obtain the minimum thickness required to produce a capillary pressure–saturation relationship independent of thickness (24 μm in the study reported here), and use this thickness for the remainder of our simulations. The saturation value corresponding to the first layer of the fibers in a 24-micron-thick coating being submerged (here 0.995), is then used to obtain the critical pressure for simulations conducted for coatings with different microstructural parameters. A vertical line is drawn for Figures 3.7a and 3.7b at this saturation level to accentuate the applicability of the clarity of the orthogonal coatings to the random.

We also investigated the effect of thickness on our defined critical pressure for the random-fiber coatings. The circles on the curves of Figure 3.7b represent the critical pressure values for the respective thicknesses corresponding to the equivalent saturation of a

submerged first layer. The inconsistency in their behavior is explained by the size distribution of the inter-fiber spaces not being statistically consistent in coatings of such low thickness.

3.5.1 DC-Electrospun Fibers

This subsection presents the results of our parameter study for coatings with random in-plane fiber orientation. Figure 3.8 illustrates the dependence of critical pressure on each of the first four terms of Equation 3.9. For better illustration and the sake of brevity, we present only the critical pressure values themselves, plotted against the varied properties. Note that the scale shown along the y-axis is the same for all plots, making the relative effect of each parameter over the others more clearly visible. For Figure 3.8a, critical pressure increases with SVF. This result can be expected because, when all other microstructural parameters are held constant, a greater population of fibers in a given volume will result in smaller inter-fiber voids, thereby raising the necessary pressure to penetrate the coating.

For Figure 3.8b, coarse and fine fiber diameter are both varied, but the ratio between them remains constant, illustrating the general dependence of pressure on the fibers' size. Obviously, the smaller the fibers, the stronger will be the coating's resistance to hydrostatic pressure. In Figure 3.8c, the diameter of the fine fibers is held constant, while the diameter of the coarse fibers is varied, in order to establish the effect of the diameter difference between the fibers used in the coating. In both the cases of Figures 3.8b and

3.8c, smaller fibers in a given domain will require more fibers to be present for the same SVF and thickness. This in turn results in the spaces between the fibers being more constrictive, yielding a higher critical pressure for the medium.

Figure 3.8d illustrates the effect on pressure response when the coarse fibers comprise more of the population in the domain. As can be seen, even for a low n_c such as 0.1, the critical pressure falls markedly with increasing n_c. This effect is accounted for by the same driving principle as for Figures 3.8b and 3.8c. A larger population of coarse fibers causes more of the given solid volume to be consolidated into fewer fibers, thereby opening the bottlenecks in the medium that would otherwise restrict water intrusion. One may therefore be compelled to infer that a bimodal design would not be an optimal choice in a superhydrophobic coating. Note, however, that there are two mechanisms that cause a superhydrophobic surface to depart from the Cassie state: failure of the meniscus under excessive hydrostatic pressures (i.e., critical pressure), and dissolution of the entrapped air in water over time. The latter can be improved by storing more air in the pores of the coating. Without larger fibers running through the medium to encourage the presence of voids therein, a smaller reserve volume of air would be taken with the coating upon submergence, reducing its lifespan against dissolution of air into the surrounding water (Samaha *et al.*, 2011).

3.5.2 AC-Electrospun Fibers

As was mentioned earlier, the high degree of order in the orthogonally layered structures results in more uniform and constrictive spaces between the fibers, facilitating a significant rise in failure pressure for the coatings compared to their randomly oriented counterparts. However, this increased order also has several noteworthy effects on pressure dependence on other structural properties. An additional effect to take into consideration is the accuracy of the electrospinning apparatus in laying down evenly spaced fibers in a given layer (the motivation for implementing Equation 3.1 in our simulation methodology). Depending on how much the fibers in a layer are allowed to deviate from their would-be positions of even spacing in a structure of given properties, the bottleneck for water penetration into a coating may not be the first layer of fine fibers.

Figure 3.9 is an example illustrating this point for the case of a set of coatings with constant microstructural parameters, varying only in the magnitude of deviation permitted in fiber spacing. When fibers are perfectly uniformly spaced, the bottleneck will invariably be the first layer of the coating. When randomness in fiber spacing is permitted to a degree of half the solution of Equation 3.1, the most constrictive layer will still be one comprised of fine fibers, but it may not occur until the second layered pair of such fibers. When fiber spacing fluctuates according to Equation 3.1, the first layer comprised of coarse fibers may also begin to contribute to the bottleneck effect, hence the increased stepwise progression shown for such a case in Figure 3.9. Precisely at what levels of fluctuation the likelihood of the bottleneck begins to vary from one layer to another depends heavily on the fiber

properties and populations for a given coating. Figure 3.9 illustrates only the example case of a coating with parameters typical of our structures, and no general trends across all coatings should be inferred. For the orthogonal coating results presented in this section, the procedure outlined in Section 3.3 was implemented, Equation 3.1 with upper limits placed on the magnitude of δ.

Figure 3.10, like Figure 3.8, displays the effect of the first four parameters in the right hand side of Equation 3.9 on critical pressure, but for the case of orthogonal layers. In generating these structures, unlike our random geometries, the rigid order in fiber orientation necessitates a different approach in characterizing their microstructural properties, in which n_c and SVF are directly obtained based on number of fibers, as opposed to mass of fibers. Consequently, additional care was required to ensure that SVF would not vary more than one percent from its intended value as a result of the number of fibers in the domain. This was done by selecting the data points to be tested for one parameter or another such as to produce structures that could retain the prescribed SVF while adjusting the other parameters. Regarding the behavior of pressure for the orthogonal case, many of the plots demonstrate the same behavior as the random media, but at higher pressure values. The presentation of Figure 3.10d varies slightly from its random counterpart in Figure 3.8d, as it does not contain information for $n_c = 0$ or 1. This is because, unlike the placement of fibers in our random media, which is inconsequential, fibers of different sizes are separated into layers, negating unimodal orthogonal structures for use as a direct comparison. Furthermore, no data is presented beyond $n_c = 0.5$. The

reasoning for this is that in such a scenario, fine fibers would no longer form the more constrictive layers within the medium, and the overall relaxing of the bottleneck effect makes such a region of operation unappealing, as can be seen in Figures 3.10a, 3.10b, and 3.10c.

It is worth mentioning that the orthogonally oriented bimodal structures examined thus far have been arranged such that two adjacent layers would consist of one fiber diameter, and the next two layers would consist of the other. As a result, both fiber diameters are oriented in both directions. However, if fiber size were alternated with every layer, all fibers of a given diameter will face the same direction, with all fibers of the other size lying perpendicular to them. Such an arrangement is expected to cause a different distribution in the size and spacing of the inter-fiber voids. Furthermore, for a bimodal fibrous coating with constant microstructural characteristics, critical pressure may still vary based on which size fibers are laid as the outer layer.

3.5.3 Further Comparisons and Optimizations

Having established the performance characteristics of the different methods, it is possible to use different permutations in design to optimize a coating's performance and cost-effectiveness. To illustrate this, a numerical test was conducted on the performance of a hybrid bimodal structure representing an 8-micron-thick coating of AC-electrospun fibers layered on top of randomly oriented fibers produced via DC electrospinning, which are easier and less time consuming to produce than their AC counterpart. Figure 3.11

illustrates the effectiveness of the orthogonal layer as a bottleneck for the entire coating. When the random layer is on the outer surface, the critical pressure for the coating is 95 kPa , whereas critical pressure is 252 kPa with the orthogonal layer on the surface. Regardless of which layer is on top, the resistance provided when the fluid interface front reaches the orthogonal layer is clearly distinguishable, as the dashed curve conforms to the solid curve. Such a coating illustrates how this process can utilize the advantages sought in both fabrication methods, providing an abundant reserve air inventory, as well as an elevated resistance to hydrostatic pressure.

3.6 Conclusions for Electrospun Nano-Fiber Coatings

In this chapter, a numerical simulation strategy was developed and used to predict the hydrostatic pressure tolerances of various bimodal, nanofibrous, superhydrophobic coatings produced via DC or AC electrospinning. The Full-Morphology approach was employed in order to examine the role of a coating's microstructural parameters in its performance. Our results show that for structures with the same solid volume fraction, coarse and fine fiber diameter, and coarse fiber population, varying only in the orientation of their fibers, the parametric controllability of our coatings produced via AC electrospinning yields significantly higher resistance to water intrusion, due to their more ordered pore structure. The influence of the particulars of a coating's microstructure is such that, from the perspective of pressure tolerance, a lower volume of empty space—and more constrictive spaces where they exist—is advantageous. Our results show that this is best achieved through the production of coatings with comparatively low porosity,

comprised predominantly, if not exclusively, of smaller fibers. However, more and larger inter-fiber gaps are still desirable for maintaining a reserve air volume for coating longevity. An example combining the elevated tolerance of the AC method and the cost-effectiveness of the DC method has been found in a coating comprised of an arbitrary volume of DC-electrospun nanofibers, with a thin coat of AC nanofibers on top. The coating fabrication methodology presented and investigated in this chapter demonstrates a viable alternative manufacturing process for superhydrophobic coatings, with performance to match those produced using more intensive and expensive techniques.

We also presented a comprehensive comparison between the predictions the FM method, our force balance formulations, and the equations of Tuteja *et al*. (2008) for fibrous coating comprised of equally spaced parallel fibers. It was found that predictions of the FM method deviates from that of the force balance method when contact angle is different from 120 degrees, but is reasonably accurate in accounting for the effects of SVF variation. The predictions of the robustness angle was found to be in close agreement with our force balance method when either SVF or contact angle were varied. The robustness height model, on the other hand, was found to be accurate only when the SVF is close to 18%.

Table 3.1: Default coating microstructure properties used in our parameter study (Section 3.5). Parameters not being varied for study will correspond to this table.

	Randomly Oriented	**Orthogonally Oriented**
Dimensions (μm)		
Solid volume fraction (%)	10.0	11.2
Coarse fiber diameter (nm)	500	500
Fine fiber diameter (nm)	100	100
Coarse fiber number fraction	0.1	0.1
Surface tension (N/m)	0.07275	0.07275
Water contact angle (deg.)	120	120

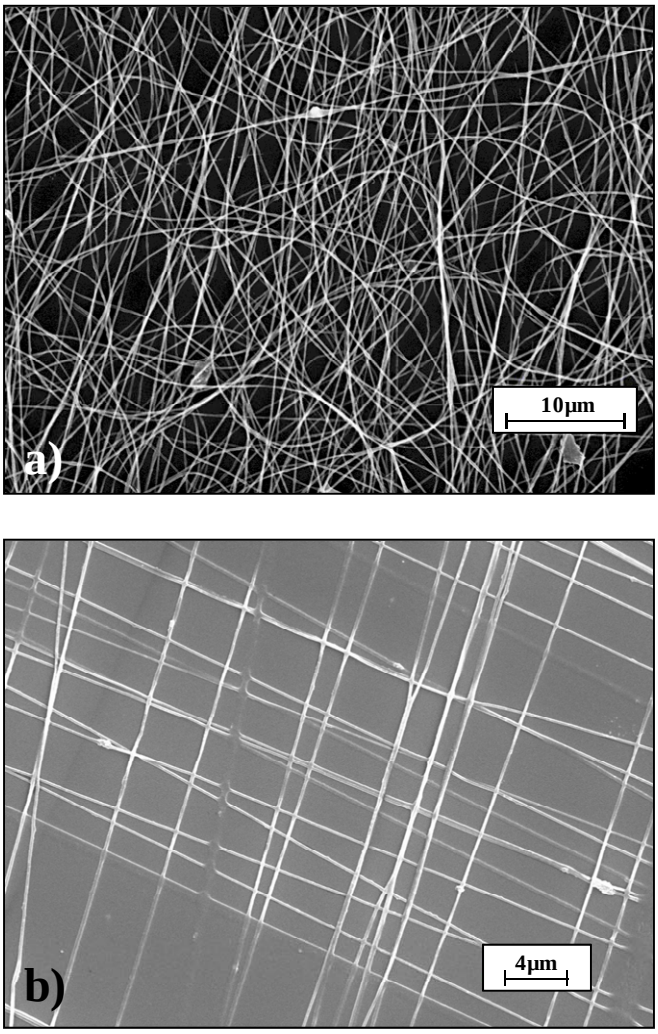

Figure 3.1: SEM images of electrospun nanofibrous coatings fabricated using: (a) DC electrospinning, (b) AC electrospinning. Our ability to produce these structures is the basis for our numerical study.

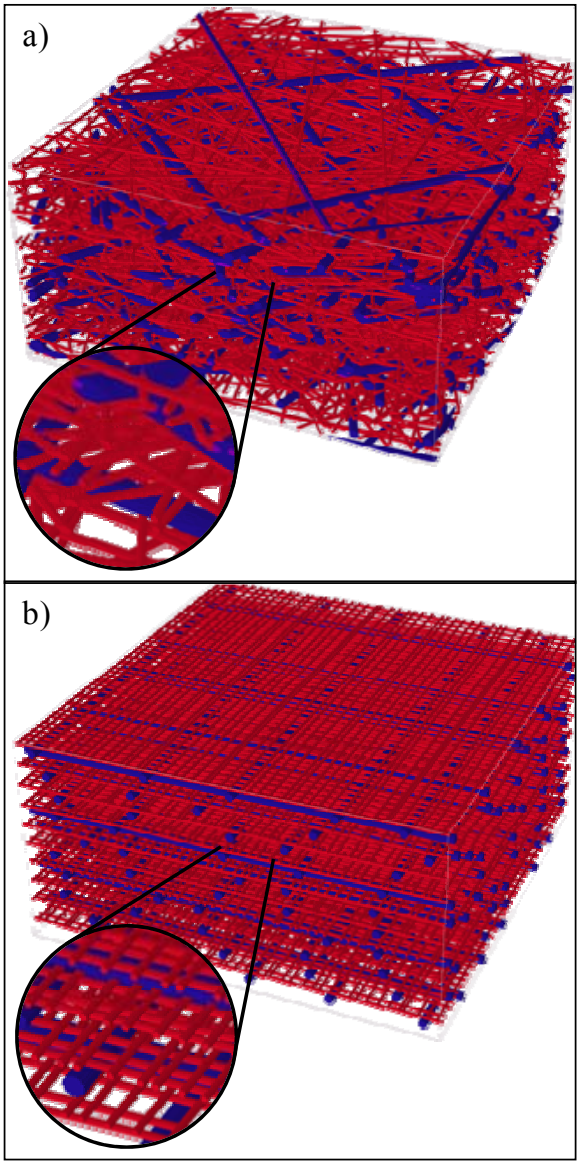

Figure 3.2: Samples of our virtual, three dimensional, bimodal fibrous structures used in our numerical study, comprised either of: (a) layered, randomly oriented fibers like those produced via DC electrospinning (SVF = 10%, df = 100 nm, Rcf = 3, nc = 0.1, t =9.6 µm) , or (b) layered, orthogonally oriented fibers like those produced via the biased AC method (SVF = 11.2%, df = 100 nm, Rcf = 3, nc = 0.1, t =9.6 µm).

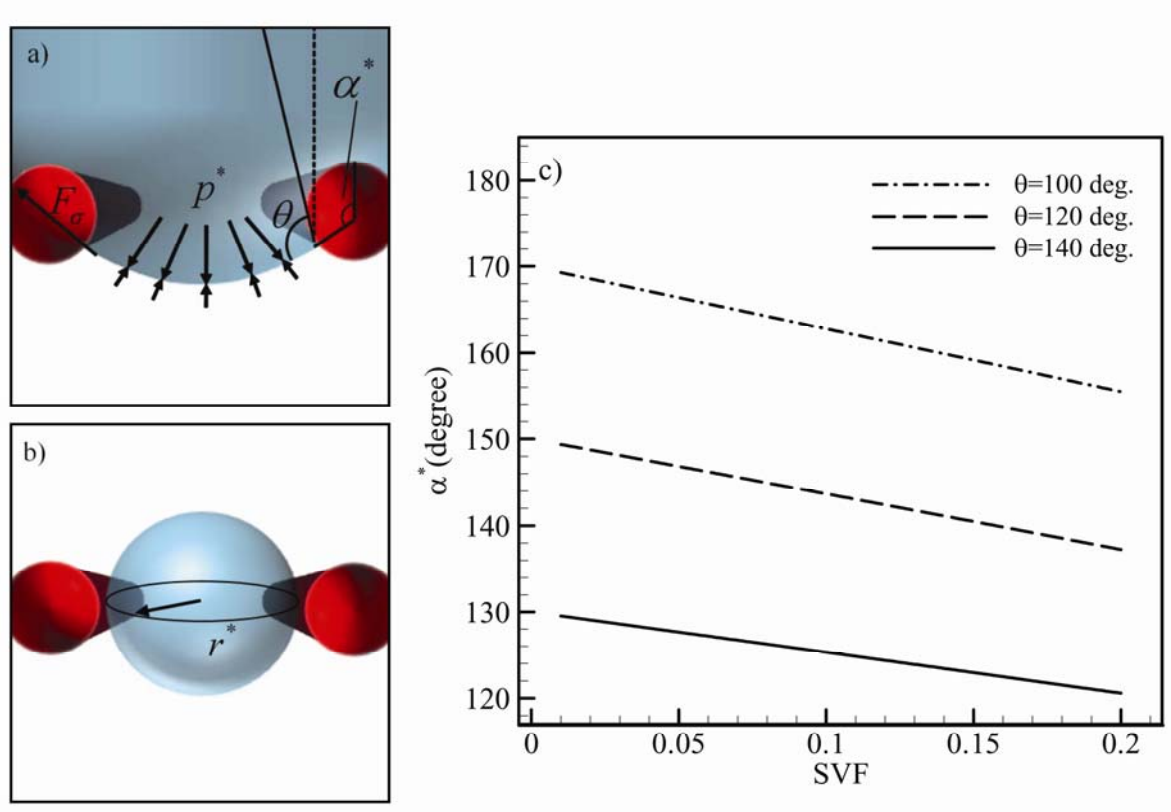

Figure 3.3: A visualization depicting the conceptual characterization of critical pressure for the case of ordered parallel fibers using the: (a) force balance and (b) FM approaches. The value of α^* associated with the force balance method is plotted (c) as a function of SVF for different contact angles.

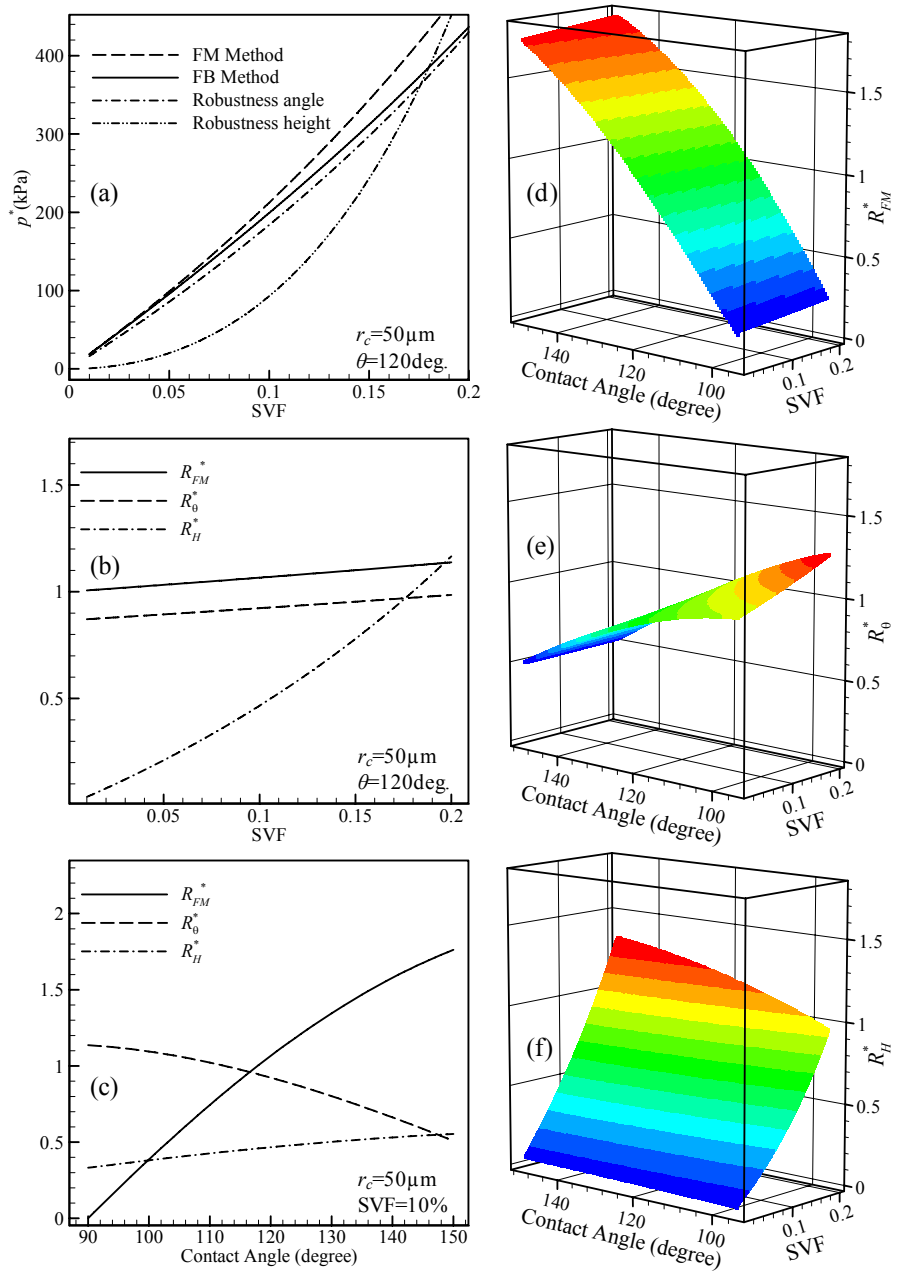

Figure 3.4: (a) Critical pressure as a function of SVF using four different methods: our force balance (FB), Full-Morphology (FM), and the robustness angle and robustness height method of Tuteja *et al.* (2008). (Equations 5, 6, 7, and 8, respectively). (b) The ratios R^*_{FM}, R^*_θ, and R^*_H as a function of SVF. (c) The ratios of R^*_{FM}, R^*_θ, and R^*_H as a function of contact angle. (d–f) Surface contour plots of R^*_{FM}, R^*_θ, and R^*_H versus SVF and contact angle.

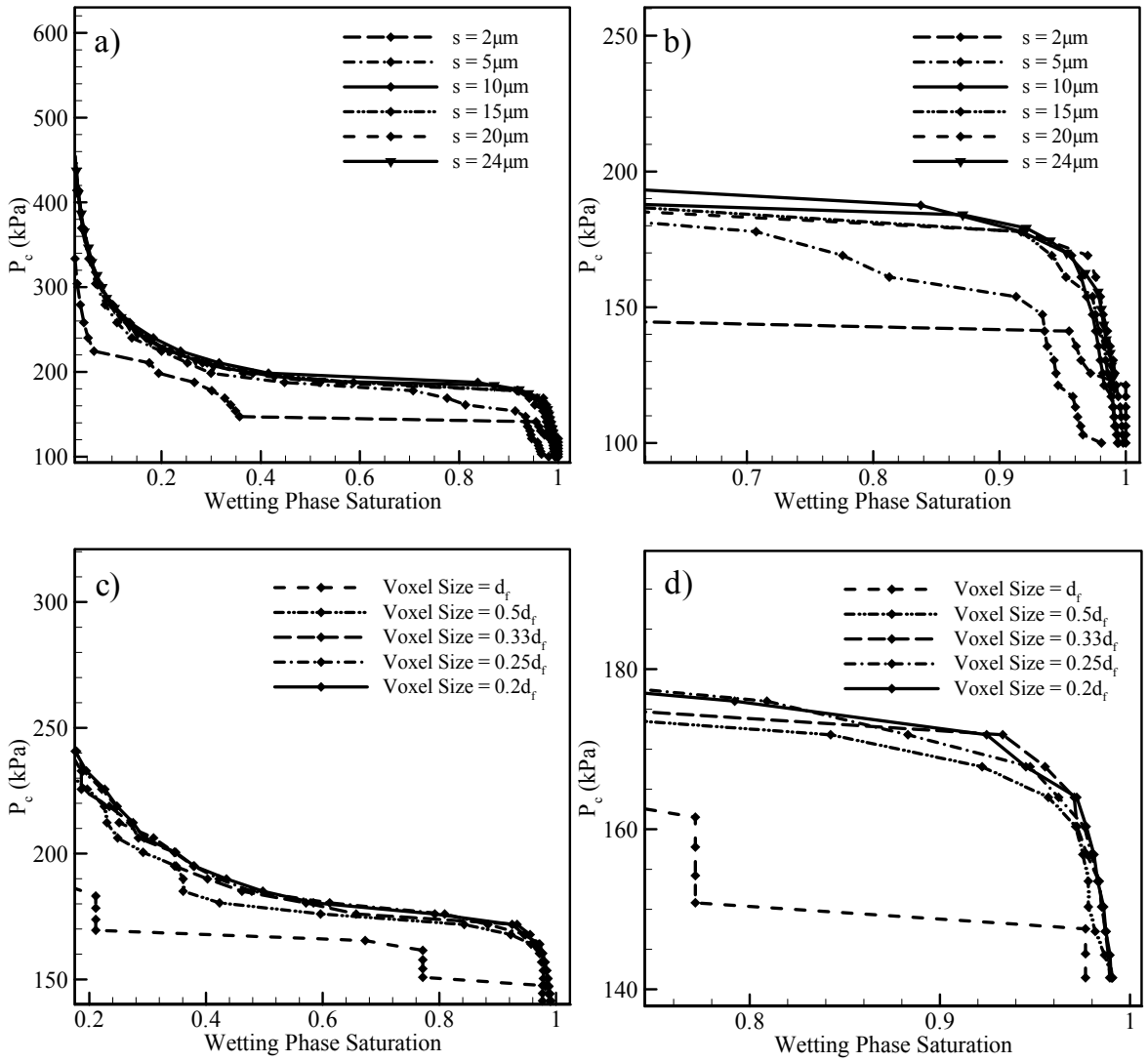

Figure 3.5: Capillary pressure–saturation curves for randomly oriented, layered structures. (a) and (b) vary only in the size of their domain (cubes of side length s); (c) and (d) vary only in their voxel resolution. Domain-size independence is acknowledged when breakthrough pressure, magnified for clarity in (b), no longer varies appreciably from one domain size to the next, taken as being greater than 10 μm. Voxel-size independence is acknowledged when critical pressure, magnified for clarity in (d), no longer varies appreciably from one voxel resolution to the next, taken as being when one voxel length is less than $0.33\,d_f$.

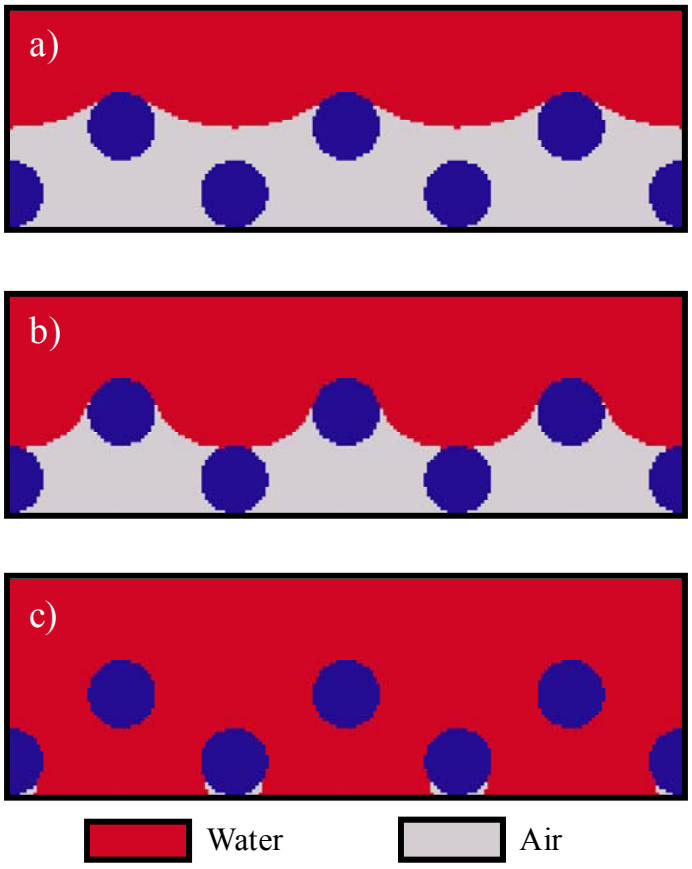

Figure 3.6: Conceptual illustration of different stages of water penetration into a coating surface, the red region representing the intruding water front: a) water has not yet fully penetrated into the first layer, b) interface has reached the second layer, but has not yet submerged the first (critical pressure is the maximum pressure value for this condition), c) coating failure has occurred; the first layer of fibers is fully submerged.

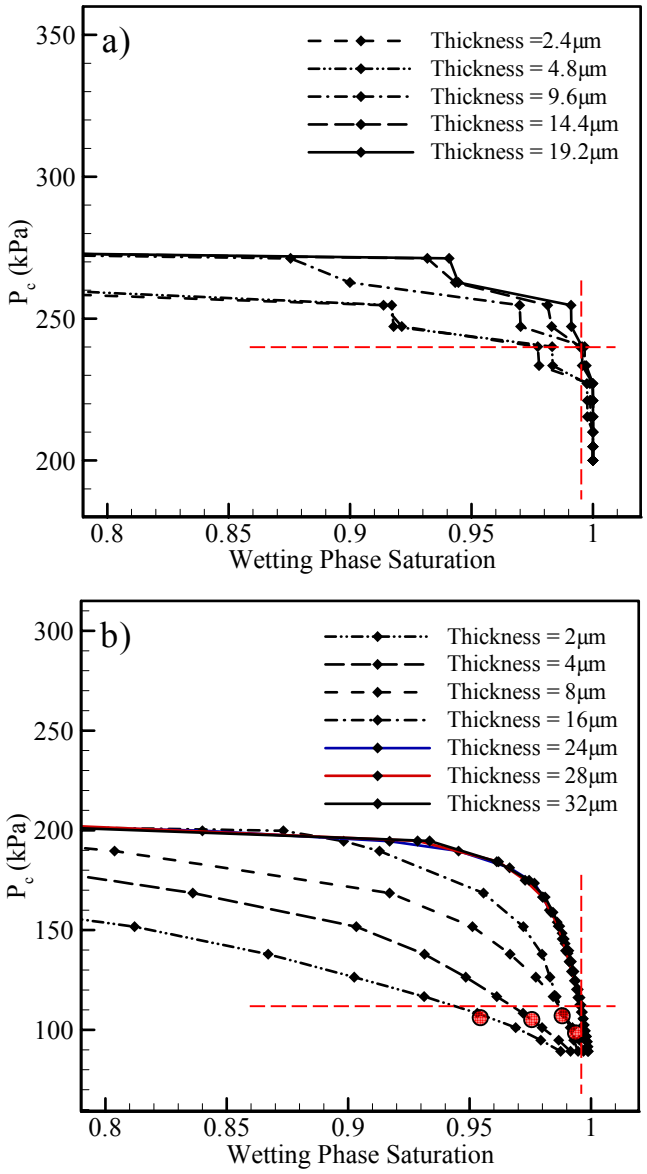

Figure 3.7: Capillary pressure–saturation curves for bimodal fibrous coatings of varying thickness comprised of: a) orthogonally oriented fibers (SVF = 11.2%, d_f = 100 nm, R_{cf} = 3, n_c = 0.1), b) randomly oriented fibers (SVF = 10%, d_f = 100 nm, R_{cf} = 3, n_c = 0.1). The dotted red cross through each plot is to better illustrate the p_c value taken as the critical pressure for the respective coating type, once thickness independence has been established. Red circles in (b) correspond to critical pressure determined for coatings not yet thickness-independent.

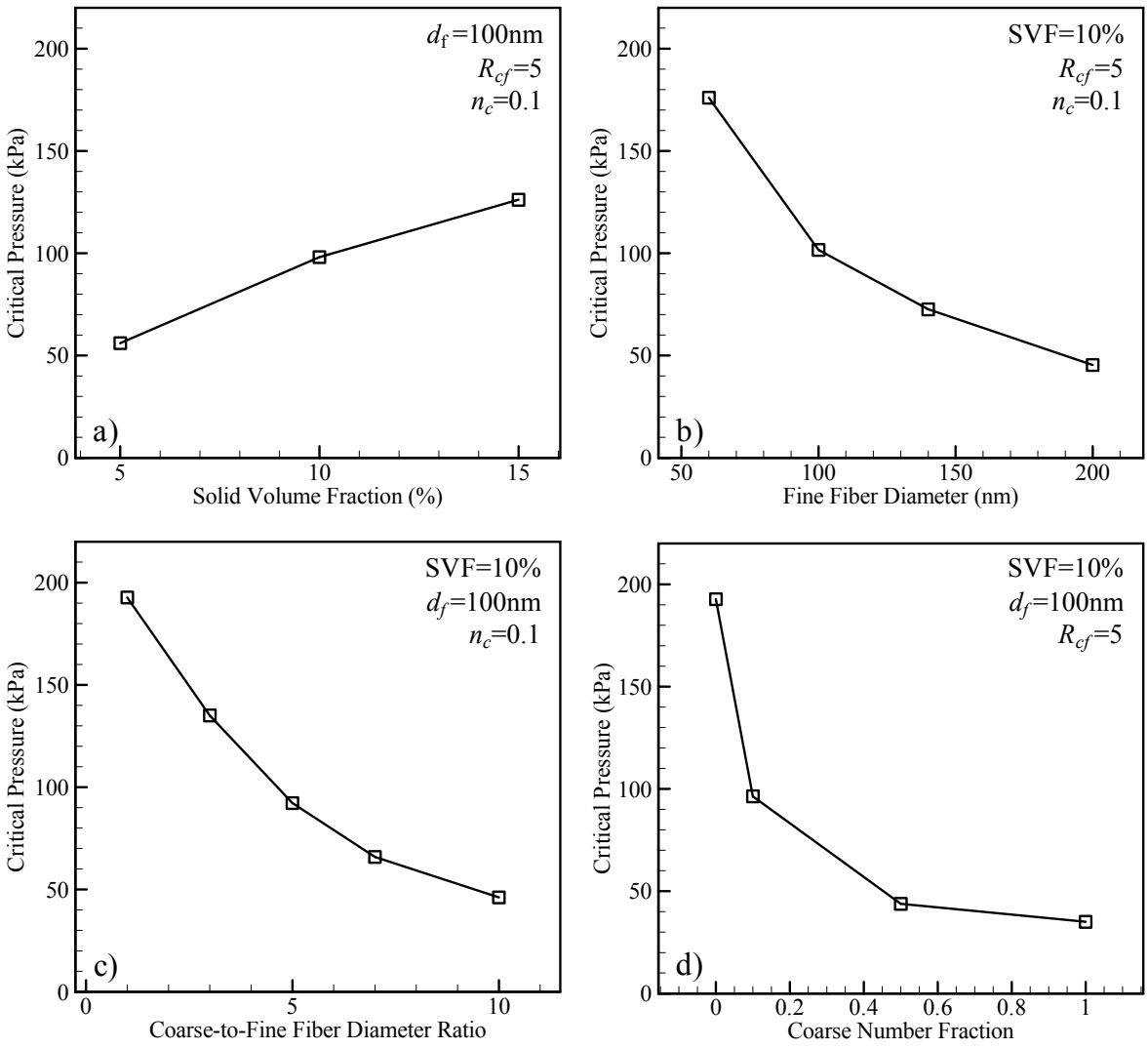

Figure 3.8: Critical pressure predictions for layered, randomly oriented (DC-electrospun) media compared against variations in one of four microstructural parameters: (a) SVF, (b) fiber diameter (holding the diameter ratio between the two fiber sizes constant), (c) coarse-to-fine fiber diameter ratio (holding fine fiber diameter constant), and (d) coarse-fiber number fraction.

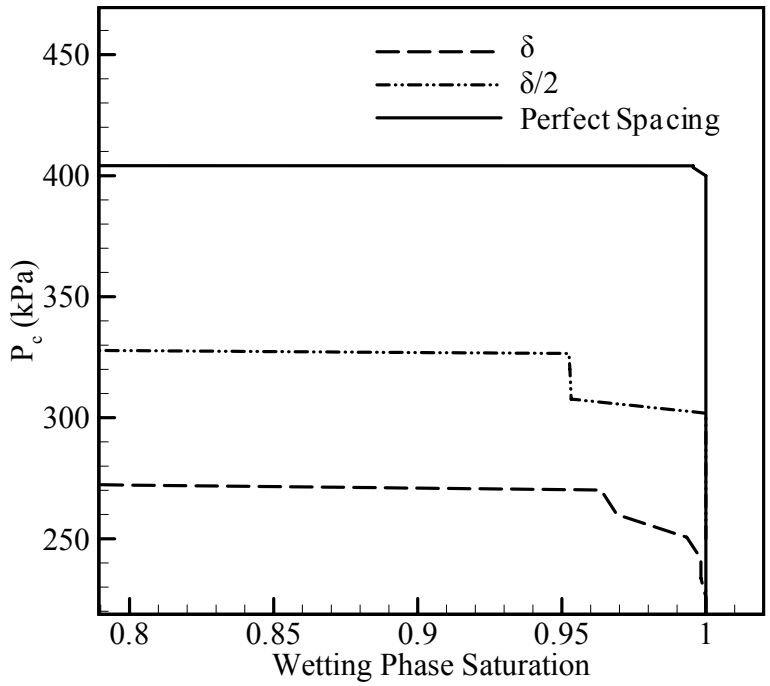

Figure 3.9: Example of capillary pressure–saturation curves for layered, orthogonally oriented structures with SVF = 11.2%, d_f = 100 nm, R_{cf} = 5, and n_c = 0.1. The structures vary only in the magnitude of each fiber's departure from 'perfectly ordered', even spacing within a layer (Equation 1).

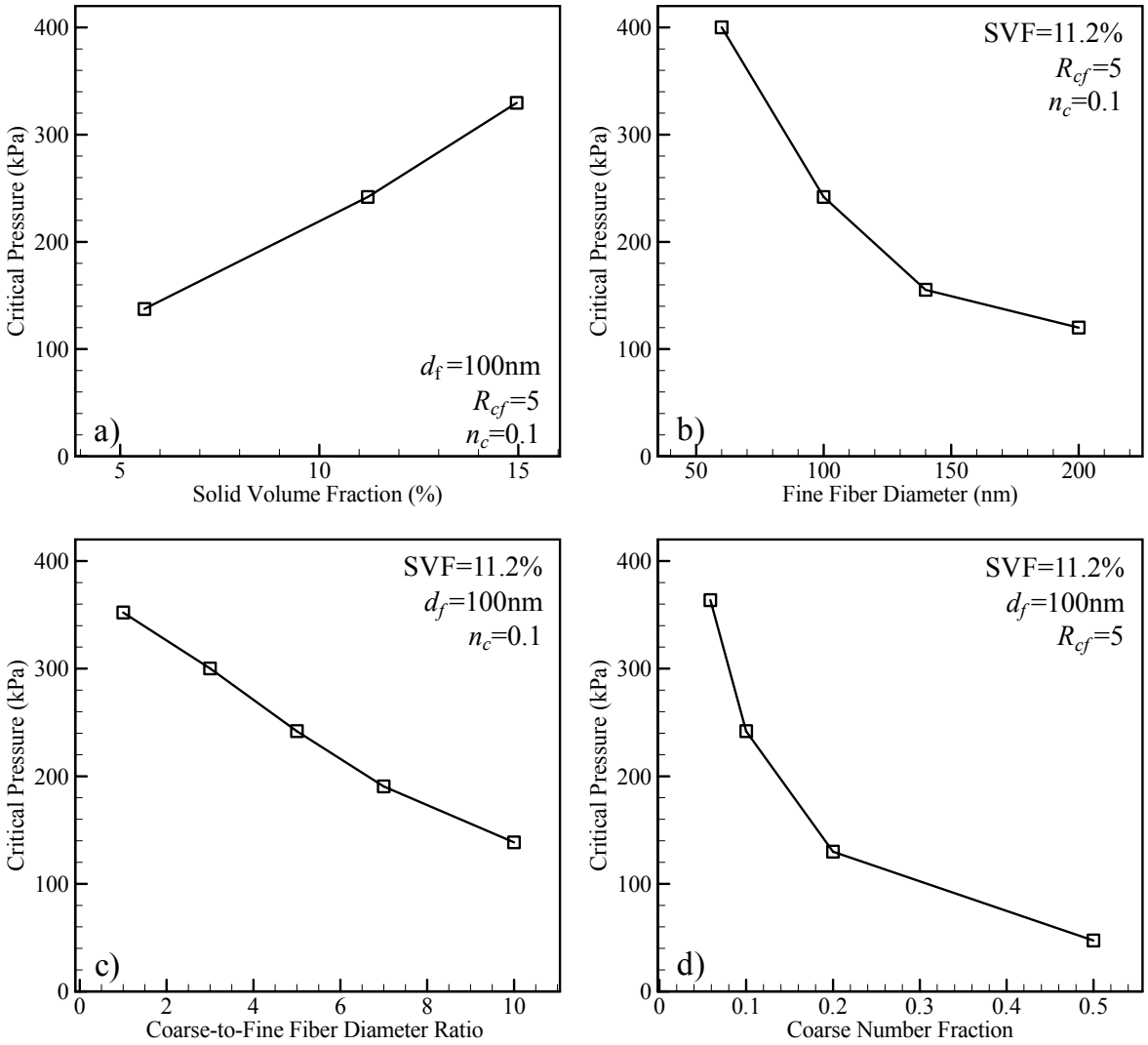

Figure 3.10: Critical pressure predictions for layered, orthogonally oriented (AC-electrospun) media compared against variations in one of four microstructural parameters: (a) SVF, (b) fiber diameter (holding the diameter ratio between the two fiber sizes constant), (c) coarse-to-fine fiber diameter ratio (holding fine fiber diameter constant), and (d) coarse-fiber number fraction.

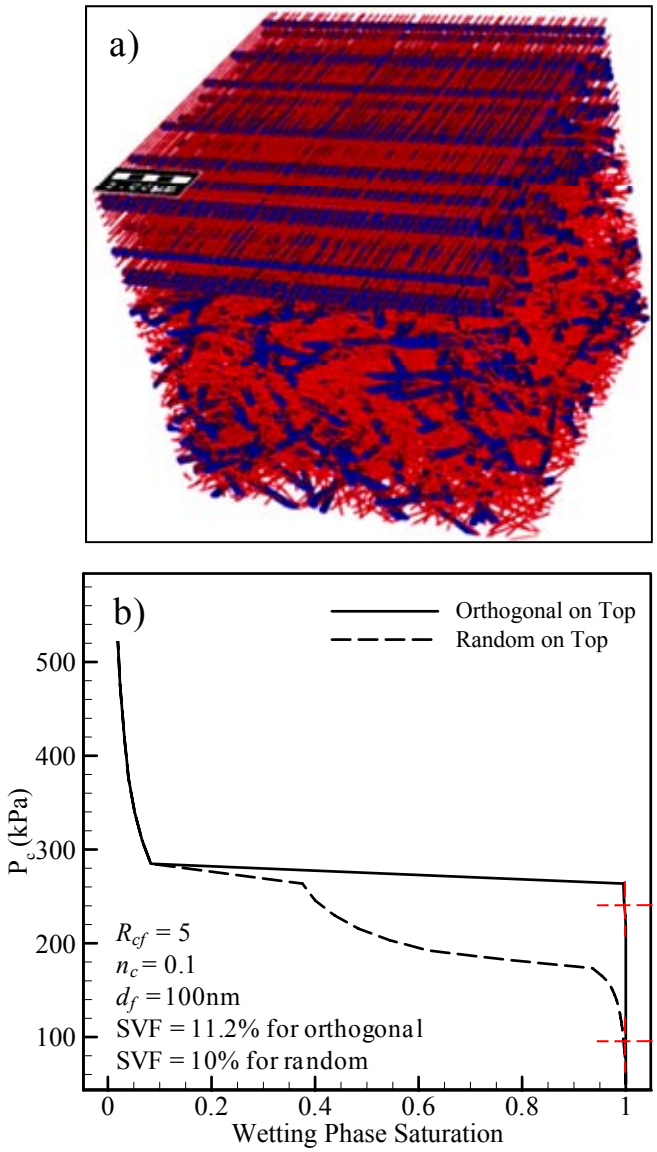

Figure 3.11: (a) An image of a hybrid coating, consisting of a 7.8-micron-thick layer of anisotropic-orthogonal fibers, and a 16.2-micron-thick layer of randomly oriented fibers, and (b) its capillary pressure–saturation curve, illustrating the difference in coating behavior depending on which layer is used as the top layer. The dashed crosses correspond to the critical pressure for each curve.

CHAPTER 4 Overall Conclusion and Future Work

In this thesis, we have established the effectiveness of the Full-Morphology method in predicting stability of superhydrophobic coatings comprised either of randomly deposited aerogel particles or electrospun nano-fibers. Coatings produced in such a manner, while inexpensive when compared to surfaces with ordered, microfabricated posts, possess a random surface roughness, and therefore do not avail themselves to solutions via analytical expressions. The FM method serves as an effective tool for predicting the critical pressure for such coatings, when no analytical correlations apply.

We have also derived analytical expressions for simple cases such as ordered posts, ordered spheres, and ordered parallel fibers, based on the balance of forces across the water–air meniscus between two solid bodies. The FM method has been compared to these analytical functions where possible, and reasonable agreement has been observed in all cases, with FM tending to slightly over-predict critical pressure for lower SVFs. For the case of parallel fibers, we have also compared our FM method and our force-balance formula with the equations of Tuteja *et al.* (2008), and discussed the differences.

Our results for both particles and fibers show that coatings have an overall higher resistance to pressure when SVF is higher and particle/fiber diameter is lower. This is because such an arrangement of properties results in more closely packed solid volume for meniscus stability, and smaller water-contact surface area where solid structures exist (greater surface roughness on the micro-scale). For our nano-fibrous structures, our results show that coatings produced via DC-biased AC electrospinning have a higher overall resistance to hydrostatic pressure, due to the smaller and less randomly sized spaces between the fibers and layers for a given set of parameters. Also, due to the tighter void-space distribution in the AC-spun coatings, coating failure occurs much more suddenly upon passing critical pressure, rather than its transition being spread across a wider pressure range. Finally, regarding bimodality in nano-fiber coatings, it has been concluded that larger coarse fibers—and more of them in a coating—result in lower critical pressure for a given SVF, as given solid volume is consolidated into fewer fibers, thereby "opening the pores" in the coating.

While still an approximation of critical pressure, the modeling methodology presented here is a nonetheless effective means for predicting the resistance of superhydrophobic coatings with random microstructures. For the case of fibers, the only analytical expression derived was that for parallel cylinders (fibers). Deviating to the case of randomly oriented fibers, even just slightly random, negates the use of that expression. A logical next step in this research could be to extend the force-balance correlations to more complicated pore geometries to help expand the applicability of analytical functions. For example, one

could develop expressions for non-parallel cylinders that have polygonal intersections with one another, e.g., a triangle or quadrilateral. By developing such expressions, one may be able to better analytically characterize more complex intersections in a coating, and better close the gap between numerical and analytical study, perhaps even distributing different correlations locally across a coating to better determine meniscus stability.

References

List of References

A. Alizadeh, M. Yamada, R. Li, W. Sheng, S. Otta, S. Zhong, L. Ge, A. Dhinojwala, K.R. Conway, V. Bahadur, A.J. Vinciquerra, B. Stephens, and M.L. Blohm, "Dynamics of ice nucleation on water repellent surfaces," Langmuir **28**, 3180–3186.

A. Ashari, T.M. Bucher, H.V. Tafreshi, M.A. Tahir, and M.S.A. Rahman, "Modeling fluid spread in thin fibrous sheets: effects of fiber orientation," Int. J. Heat Mass Tran. **53**, 1750 (2010).

A. Ashari and H.V. Tafreshi, "General capillary pressure and relative permeability expressions for through–plane fluid transport in thin fibrous sheets," Colloid Surface A **346**, 114 (2009).

W. Barthlott and C. Neinhuis, "Purity of the sacred lotus, or escape from contamination in biological surfaces," Planta **202**, 1–8 (1997).

J. Becker, V. Schulz, A. Wiegmann, "Numerical determination of two-phase material parameters of gas diffusion layer using tomography images," J. Fuel Cell Sci. Technol. **5**, 021006 (2008).

B. Bhushan, "Bioinspired structured surfaces," Langmuir **28**, 1698–1714 (2012).

A. B. D. Cassie, and S. Baxter, "Wettability of porous surfaces," Transactions of the Faraday Society **40**, 546 (1944).

R. J. Daniello, N. E. Waterhouse, and J. P. Rothstein, "Drag reduction in turbulent flows over superhydrophobic surfaces," Physics of Fluids **21**, 085103 (2009).

J. Davies, D. Maynes, B. W. Webb, and B. Woolford, "Laminar flow in microchannel with superhydrophobic walls exhibiting transverse ribs," Physics of Fluids **18**, 087110 (2006).

D.A. Doshi, P.B. Shah, S. Singh, E.D. Branson, A.P. Malanoski, E.B. Watkins, J. Majewski, F. van Swol, C.J. Brinker, "Investigating the interface of superhydrophobic surfaces in contact with water," Langmuir **21,** 7805–7811 (2005).

F.A.L. Dullien, "Porous Media Fluid Transport and Pore Structure," 2nd edition, Academic Press, San Diego (1992).

B. Emami, H.V. Tafreshi, M. Gad-el-Hak, and G.C. Tepper, "Predicting shape and stability of air-water interface on superhydrophobic surfaces with randomly distributed, dissimilar posts," Appl. Phys. Lett. **98** 203106 (2011).

B. Emami, H.V. Tafreshi, M. Gad-el-Hak, and G.C. Tepper, "Effect of fiber orientation on shape and stability of air–water interface on superhydrophobic electrospun thin coatings," J. App. Phys **111**, 064325 (2012).

P. Forsberg, F. Nikolajeff, and M. Carlsson, "Cassie–Wenzel and Wenzel–Cassie transitions on immersed superhydrophobic surfaces under hydrostatic pressure," Soft Matter **7** 104–109 (2011).

M. Gad-el-Hak, "Flow Control: Passive, Active, and Reactive Flow Management," Cambridge University Press, London, United Kingdom (2000).

P. Gao, and J. J. Feng, "Enhanced slip on a patterned substrate due to dipinning of contact line," Physics of Fluids **21**, 102102 (2009).

R.D. Hazlett, "Simulation of capillary–dominated displacements in microtomographic images of reservoir rocks," Transport Porous Med. **20**, 21 (1995).

M. Hilpert and C.T. Miller, "Pore-morphology-based simulation of drainage in totally wetting porous media," Adv.Water Resour. **24**, 243 (2001).

S.A. Hosseini and H.V. Tafreshi, "Modeling permeability of 3-D nanofiber media in slip flow regime," Chem. Eng. Sci.**65**, 2249–2254 (2010).

http://www.greendiary.com/gallery/diving-bell-spider

http://commons.wikimedia.org/wiki/File:Water-strider-1.jpg

http://yvesrubin.photoshelter.com/image/I0000K.Kp5rcER18

S. Jaganathan, H.V. Tafreshi, and B. Pourdeyhimi, "Modeling liquid porosimetry in modeled and imaged 3-D fibrous microstructures," J. Colloid Interf. Sci. **326** 166–175 (2008).

S. Jaganathan, H.V. Tafreshi, and B. Pourdeyhimi, "A realistic modeling of fluid infiltration in thin fibrous sheets," J. Appl. Phys. **105**, 113522 (2009).

R. Kessick and G. Tepper, "Electrospun polymer composite fiber arrays for the detection of volatile organic compounds," Sensor. Actuat. B-Chem. **117** 205–210 (2006).

R. Kessick and G. Tepper, "Microscale polymeric helical structures produced by electrospinning," Appl. Phys. Lett. **84**, 4807–4809 (2004).

R. Kessick and G. Tepper, "Microscale electrospinning of polymer nanofiber interconnections," Appl. Phys. Lett. **83**, 557–559 (2003).

K. Koch, B. Bhushan, Y.C. Jung, W. Barthlott, "Fabrication of artificial lotus leaves and significance of hierarchical structure for superhydrophobicity and low adhesion," Soft Matter **5**, 1386–1393 (2009).

E. Lauga, and H. A. Stone, "Effective slip in pressure-driven Stokes flow," J. Fluid Mech. **489**, 55 (2003).

C. Lee, C.H. Choi, and C. J. Kim, "Structured surfaces for giant liquid slip," Phys. Rev. Lett. **101**, 064501 (2008).

C. Lee and C.J. Kim, "Maximizing the giant liquid slip on superhydrophobic microstructures by nanostructuring their sidewalls," Langmuir **25,** 12812 (2009).

N. Levit and G. Tepper, "Supercritical CO_2-assisted electrospinning," J. Supercrit. Fluid **31**, 329–333 (2004).

E.J. Lobaton, T.R. Salamon, Computation of constant mean curvature surfaces: application to the gas–liquid interface of a pressurized fluid on a superhydrophobic surface, J. Colloid Interf. Sci. **314**, 184–198 (2007).

M.L. Ma, R.M. Hill and G.C. Rutledge, "A review of recent results on superhydrophobic materials based on micro- and nanofibers," J. Adhes. Sci. Technol. **22**, 1799–1817 (2008).

M.L. Ma, Y. Mao, M. Gupta, K.K. Gleason, and G.C. Rutledge, "Superhydrophobic fabrics produced by electrospinning and chemical vapor deposition," Macromolecules **38,** 9742–9748 (2005).

A. Marmur, "Underwater superhydrophobicity: theoretical feasibility," Langmuir, **22**, 1400–1402 (2006).

M. B. Martell, J. B. Perot, and J. P. Rothstein, "Direct numerical simulations of turbulent flows over superhydrophobic surfaces," Journal of Fluid Mechanics **620**, 31 (2009).

D. Maynes, K. Jeffs, B. Woolford, and W. Webb, "Laminar flow in a microchannel with hydrophobic surface patterned microribs oriented parallel to the flow direction," Physics of Fluids **19**, 093603.1 (2007).

B. Maze, H.V. Tafreshi, and B. Pourdeyhimi, "Geometrical modeling of fibrous materials under compression," J. Appl. Phys. **102**, 073533 (2007a).

B. Maze, H.V. Tafreshi, Q. Wang, and B. Pourdeyhimi, "Unsteady–state simulation of nanoparticle aerosol filtration via nanofiber electrospun filters at reduced pressures," J. Aerosol Sci. **38**, 550–571 (2007b).

C.L.M.H. Navier, "Memoire sur les lois du movement des fluides," Mem. Acad. R. Sci. Inst. France **6**, 389–440 (1823).

F.O. Ochanda, M.A. Samaha, H.V. Tafreshi, G.C. Tepper, and M. Gad-el-Hak, "Fabrication of superhydrophobic coatings by DC-biased AC-electrospinning," J. Appl. Polym. Sci. **123**, 1112–1119 (2012a).

F.O. Ochanda, M.A. Samaha, H.V. Tafreshi, G.C. Tepper, and M. Gad-el-Hak, "Salinity effects on the degree of hydrophobicity and longevity for superhydrophobic coatings," J. Appl. Polym. Sci. **124**, 5021–5026 (2012b).

A. Okabe, B. Boots, K. Sugihara, and S.N. Chiu, "Spatial Tessellations: Concepts and Applications of Voronoi Diagrams," Wiley, Chichester (2000).

J. Ou, B. Perot, and J. P. Rothstein, "Laminar drag reduction in microchannels using ultrahydrophobic surfaces," Physics of Fluids **16**, 4635 (2004).

J. Ou, and J. P. Rothstein, "Direct velocity measurments of the flow past drag-reducing ultrahydrophobic surfaces," Physics of Fluids **17**, 103606.1 (2005).

R. Poetes, K. Holtzmann, K. Franze, and U. Steiner, "Metastable underwater superhydrophobicity," Phys. Rev. Lett. **105**, 166104 (2010).

C. Pozrikidis, "Computation of three-dimensional hydrostatic menisci," IMA J. Appl. Math. **75**, 418–438 (2010).

A.V. Rao, M.M. Kulkarni, S.D. Bhagat, "Transport of liquids using superhydrophobic aerogels," J. Colloid Interf. Sci. **285**, 413 (2005).

A.V. Rao, G.M. Pajonk, S.D. Bhagat, P. Barboux, "Influence of gel aging and Na2SiO3/H2O molar ratio on monolithicity and physical properties of water-glass-based aerogels dried at atmospheric pressure," J. Non-Cryst Solids **350**, 216(2004).

D.H. Reneker and A.L. Yarin, "Electrospinning jets and polymer nanofibers," Polymer **49**, 2387–2425 (2008).

J.P. Rothstein, "Slip on superhydrophobic surfaces", Annu. Rev. Fluid Mech. **42**, 89–109 (2010).

M.A. Samaha, F.O. Ochanda, H.V. Tafreshi, G.C. Tepper, and M. Gad-el-Hak, "In situ, non-invasive characterization of superhydrophobic coatings," Rev. Sci. Instrum. **82**, 045109 (2011a).

M.A. Samaha, H.V. Tafreshi, and M. Gad-el-Hak, "Modeling drag reduction and meniscus stability of superhydrophobic surfaces comprised of random roughness," Phys. Fluids **23**, 012001 (2011b).

M.A. Samaha, H.V. Tafreshi, and M. Gad-el-Hak, "Superhydrophobic surfaces: from the lotus leaf to the submarine," Comptes Rendus Mechanique **340**, 18–34 (2012).

S. Sarkar, S.C. Deevi, and G.Tepper, "Biased AC electrospinning of aligned polymer nanofibers," Macromol. Rapid Comm. **28**, 1034–1039 (2007).

M. Sbragaglia, and A. Prosperetti, "Effective velocity boundary condition at a mixed slip surface," J. Fluid Mech. **578**, 435 (2007).

V. Schulz, J. Becker, A. Wiegmann, P. Mukherjee, C. Wang, "Modeling of two-phase behavior in the gas diffusion medium of PEFCs via full-morphology approach," J. Electrochem. Soc. **154 (4)**, B419 (2007).

R.S. Seymour and S.K. Hetz, "The diving bell and the spider: the physical gill of *argyroneta aquatic*," J. Exp. Biol **214**, 2175–2181 (2011).

X. Sheng, J. Zhang, "Air Layer on superhydrophobic surfaces underwater," Colloid Surface A. **377,** 374–378 (2011).

A. Singh, L. Steely, and H. R. Allcock, "Poly[bis(2,2,2-trifluoroethoxy)phosphazene] superhydrophobic nanofibers," Langmuir **21**, 11604 (2005).

P. Soille, "Morphological image analysis: principal and applications," Spring Verlag, Heidelberg, 1999.

H.V. Tafreshi, M.S.A. Rahman, S. Jaganathan, Q. Wang, and B. Pourdeyhimi, "Analytical expressions for predicting permeability of bimodal fibrous porous media," Chem. Eng. Sci.**64**, 1154 (2009).

M.A. Tahir and H.V. Tafreshi, "Influence of fiber orientation on the transverse permeability of fibrous media," Phys. Fluids **21**, 083604 (2009).

R. Truesdell, A. Mammoli, P. Vorobieff, F. van Swol, and C. J. Brinker, "Drag reduction on a patterned superhydrophobic surface," Physical Review Letters **97**, 044504.1 (2006).

A. Tuteja, W. Choi, J.M. Mabry, G.H. McKinley, and R.E. Cohen, "Robust omniphobic surfaces," P Natl Acad Sci USA **105**, 18200–18205 (2008).

H. J. Vogel, J. Tolke, V. P. Schulz, M. Krafczyk, K. Roth, "Comparison of a lattice–Boltzmann model, a full-morphology model, and a pore network model for determining capillary pressure–saturation relationships," Vadose Zone J. **4**, 380 (2005).

R. N. Wenzel, "Resistance of a solid surface to wetting by water," Industrial and Engineering Chemistry **28**, 988 (1936).

A.L. Yarin, S. Koombhongse, and D.H. Reneker, "Taylor cone and jetting from liquid droplets in electrospinning of nanofibers," J. Appl. Phys. **90** 4836–4846 (2001).

Q.S. Zheng, Y. Yu, and Z.H. Zhao, "Effects of hydraulic pressure on the stability and transition of wetting modes of superhydrophobic surfaces," Langmuir **21**, 12207 (2005).

M. Zhu, W. Zuo, H. Yu, W. Yang, and Y. Chen, "Superhydrophobic surface directly created by electrospinning based on hydrophilic materials," Journal of Materials Science **41**, 3793 (2006).

Thomas M. Bucher Jr.

Email: buchertm@mymail.vcu.edu

Education

• **M.S. in Mechanical and Nuclear Engineering** (August 2012)
Virginia Commonwealth University, Richmond, VA
GPA 4.0
Thesis title: "Modeling the Resistance to Hydrostatic Pressures for Superhydrophobic Coatings Comprised of Random Roughness"

• **B.S. in Mechanical Engineering** (May 2010)
Virginia Commonwealth University, Richmond, VA
GPA 3.865 Magna Cum Laude

Research Experience

VCU Porous Media and Multiphase Flows Laboratory (May 2009–Present)

• Currently performing research in the field of aerosol filtration, modeling particle capture in nano-fibrous filter media using commercial software enhanced with in-house subroutines (user-defined functions)

• Developed numerical models for predicting absorption and drainage characteristics for 2-D and 3-D lump, composite, and layered fibrous materials. Simulation methodology is validated and refined using experimental data

• Developed numerical model for predicting the performance of granular and nano-fibrous superhydrophobic coatings under elevated hydrostatic pressure for submersible applications (subject of M.S. thesis)

Publications

• **Bucher, T.M.**, Tafreshi, H.V., "Modeling the Performance of Thin Nanofibrous Filter Coatings with Orthogonal Fiber Orientation," to be submitted to Aerosol Science and Technology

• **Bucher, T.M.**, Emami, B., Tafreshi, H.V., Gad-el-Hak, M., Tepper, G.C., "Modeling Resistance of Nanofibrous Superhydrophobic Coatings to Hydrostatic Pressures: the Role of Microstructure," Physics of Fluids 24, 022109 (2012)

• Ashari, A., **Bucher, T.M.**, Tafreshi, H.V., "Modeling Motion-Induced Fluid Release from Partially-Saturated Fibrous Media onto Surfaces with Different Hydrophilicity," International Journal of Heat and Fluid Flow 382 (5), 1076–1081 (2011)

• Emami, B., **Bucher, T.M.**, Tafreshi, H.V., Gad-el-Hak, M., Tepper, G.C., "Simulation of Meniscus Stability in Superhydrophobic Granular Surfaces under Hydrostatic Pressures," Colloids and Surfaces A: Physiochemical and Engineering Aspects 385, 95–103 (2011)

• Ashari, A., **Bucher, T.M.**, Tafreshi, H.V., "A semi-analytical model for simulating fluid transport in multi-layered fibrous sheets made up of solid and porous fibers," Computational Materials Science 50, 378 (2010)

• Ashari, A., **Bucher, T.M.**, Tafreshi, H.V., Tahir, M.A., Rahman, M.S.A., "Modeling Fluid Spread in Thin Fibrous Sheets: Effect of Fiber Orientation," International Journal of Heat & Mass Transfer 53, 1750 (2010)

Book Chapter

•Tafreshi, H.V., **Bucher, T.M.**, "Modeling Fluid Absorption in Anisotropic Fibrous Porous Media" in Wicking in Porous Materials:Traditional and Modern Modeling Approaches, eds. Pillai, K.M., and Masoudi, R. Publisher: Taylor and Francis/CRC (in preparation 2012)

Conference Proceedings

• **Bucher, T.M.**, Emami B., Tafreshi, H.V., "Modeling superhydrophobic Surfaces Comprised of Randomly Deposited Fibers or Particles," 4th International Conference on Porous Media and Annual Meeting of the International Society for Porous Media, May 14–16 (2012)

• Tafreshi, H.V., **Bucher, T.M.**, "Modeling Transport Phenomena in Anisotropic Fibrous Media," 4th International Conference on Porous Media and Annual Meeting of the International Society for Porous Media, May 14–16 (2012)

• **Bucher, T.M.**, Emami, B., Tafreshi, H.V., Gad-el-Hak, M., Tepper, G.C., "On the Resistance of Nanofibrous Superhydrophobic Coatings to Hydrostatic Pressures," Bulletin of the American Physical Society 56, no. 18, p. 175 (2011)

• **Bucher, T.M.**, Tafreshi, H.V., "An Overview on Modeling Fluid Absroption in Fibrous Media," NETinc, Innovative Nonwovens Conference, Sep 13–15 (2011), Atlanta Georgia (2011)

Journals Served as Reviewer

• Chemical Engineering Research and Design

• Journal of Nanoparticle Research

• Chemical Engineering science

• International Journal of Heat and Mass Transfer

• Separation and Purification Technology

•Aerosol Science and Technology

Research Sponsors

• National Science Foundation (January 2012–present)

• Johnson & Johnson (January 2011–December 2011)

• Defense Advanced Research Projects Agency (DARPA) (September 2010–January 2011)

• Ahlstrom (August 2010–January 2011)

Other Relevant Accomplishments

• **Mircoscale–Macroscale Fluid Absorption Model** (January 2011–December 2011)
Developed user-friendly software model for predicting the fluid-absorption and transfer performance of multiple fabric layers in feminine sanitary products based solely on the properties of the fluid and microstructure of the fabrics. Program was developed for and is currently being used as a design tool by Johnson & Johnson

• **Ph.D. Qualifying Exam** (Fall 2010)
Successfully passed the Ph.D. Qualifying Exam for the VCU Department of Mechanical and Nuclear Engineering in my first semester as a graduate student, less than six months after my baccalaureate

• **VCU Nuclear Reactor Simulator** (Fall 2009–Spring 2010)
Combined cumulative engineering knowledge with prior Navy experience, and was instrumental in the initial construction and programming of a nuclear power plant simulator that has gone on to become a training and education tool for the VCU Nuclear Engineering Program

• **Tobacco Company Restaurant** (2004–2008)
Spent the first two thirds of my undergraduate education also supporting myself and my education by working full time as a cook at the famous Tobacco Company Restaurant in Downtown Richmond

Mentorship Experience

• **Undergraduate Fluid Mechanics Independent Study** (Fall 2011–Spring 2012)
Conducted the undergraduate Fluid Mechanics course as an independent study for an undergraduate student. Duties included tutoring; writing, assigning, and grading homework assignments; and writing and conducting midterm and final exams

• **VCU Porous Media and Multiphase Flows Laboratory** (Summer–Fall 2010)
Supervised five undergraduate student workers in various design and experimental work involving several lab projects

• **Engineering Thermal Sciences Lab Teaching Assistant** (Spring 2010)
Set up weekly experiments, supervised thirty students as they conducted the experiments in small groups, and graded their subsequent lab reports, also made myself available to answer students' questions throughout the week as they wrote their reports

Professional Society

• Interpore (International Society for Porous Media)

Graduate Coursework

• Advanced Engineering Mathematics (EGRM 512)

• Vibrations (EGRM 515)

• Advanced Fluid Mechanics (EGRM 561)

• Flow Control (EGRM 580)

• Porous Media Independent Study (EGRM 692)

• Topics in Nuclear Engineering (EGRN 610)

• Nuclear Reactor Safety (EGRN 640)

• Energy Conversion Systems (EGRM 691)

• Nuclear Power Plants (EGRN 630)

• Convective Heat Transfer (EGRM 602)

Industry Experience

• **United States Naval Nuclear Propulsion Program** (1997–2001)
Orlando, FL; Ballston Spa, NY
Nuclear plant mechanical operator and instructor

Software Proficiencies

• **Engineering**
FlexPDE,Geodict, ANSYS-FLUENT, Gambit, Particle Image Velocimetry (PIV) software, Solidworks

• **Programming Languages**
Matlab, C

• **General**
LaTeX, Tecplot, SigmaPlot, Adobe Photoshop, MS Office, Linux Open Office